

Microstructure Characterization of Creep-Tested Reformer Tube Material

by

Mohd Aiman Bin Ismail

Dissertation submitted in partial fulfilment of
the requirements for the
Bachelor of Engineering (Hons)
(Mechanical Engineering)

JANUARY 2008

Universiti Teknologi PETRONAS
Bandar Seri Iskandar
31750 Tronoh
Perak Darul Ridzuan

CERTIFICATION OF APPROVAL

Microstructure Characterization of Creep-Tested Reformer Tube Material

by

Mohd Aiman Bin Ismail

A project dissertation submitted to the
Mechanical Engineering Programme
Universiti Teknologi PETRONAS
in partial fulfilment of the requirement for the
BACHELOR OF ENGINEERING (Hons)
(MECHANICAL ENGINEERING)

Approved by,

(Dr. Azmi Bin Abdul Wahab)

UNIVERSITI TEKNOLOGI PETRONAS

TRONOH, PERAK

January 2008

CERTIFICATION OF ORIGINALITY

This is to certify that I am responsible for the work submitted in this project, that the original work is my own except as specified in the references and acknowledgements, and that the original work contained herein have not been undertaken or done by unspecified sources or persons.

MOHD AIMAN BIN ISMAIL

ABSTRACT

In this project, the main objective was to study the transformation of a reformer tube material during creep by comparing the microstructure in creep-tested samples with an as-cast sample. The comparison was made in terms of the shape, average particle size, percentage particle area and additional microstructural characteristics of the creep-tested samples. Some basic characterization of creep voids was also included to study the effect of creep.

Four previously creep-tested samples were obtained from Schmidt + Clemens (Spain) for preparation and evaluation. These creep-tested samples were manufactured from the wall of a reformer tube. An as-cast sample of the reformer tube was also obtained for comparison. The samples were examined using optical microscope (OM) and scanning electron microscope (SEM) with secondary electron (SE) and backscattered electron (BSE) imaging and energy dispersive spectroscopy (EDS) was conducted at selected areas of the samples. The average particle size and percentage particle area of the primary carbides were measured by using open source NIH ImageJ software.

It was found out that the microstructure in the as-cast sample consists of an austenitic matrix with a network of two types of primary carbides determined to be chromium-rich $M_{23}C_6$ and niobium-rich NbC. Whereas that of the creep-tested samples also exhibit a fine dispersion of small needle-like structure which is the secondary carbides of $M_{23}C_6$. The fine faceted edges of the primary carbides in the as-cast sample transformed into coarser and rounder precipitates as creep progress. There were also voids observed in the creep-tested samples when compared with the as-cast sample. The average particle size and percentage area of both the $M_{23}C_6$ and NbC in the creep-tested samples decreased when compared with the as-cast sample. The average particle size of Cr and Nb in the as-cast sample decreased from 41.58 and 46.64 μm^2 to 31.39 and 9.19 μm^2 in sample 320, 25.66 and 7.37 μm^2 in sample 321, 28.65 and 4.95 μm^2 in sample 322 and, 27.19 and 9.11 μm^2 in sample 326 respectively. Meanwhile, the percentage area of Cr

and Nb in the as-cast sample decreased from 6.94 and 5.05 percents to 6.44 and 3.37 percents in sample 320, 6.92 and 2.92 percents in sample 321, 6.91 and 3.47 percents in sample 322 and, 5.75 and 3.44 percents in sample 326 respectively. The most obvious decrease in the average particle size and percentage area was in the NbC. This was believed to be due to Nb was dissolved in the steel to form new bonds such as titanium carbide, TiC.

ACKNOWLEDGEMENT

First and foremost, the highest gratitude goes to Allah the Al-Mighty because of His mercy and kindness that I have successfully completed this project within the time provided. Throughout the two semesters, it had greatly benefited me in various aspects especially in materials engineering. The experiences gained will be very useful to me in my future career. It his hoped that all the information gained from this project may benefit others especially UTP students and staffs for reference. The successful completion of this project had been made possible through the help and support of many individuals and organizations.

I would like to express my special gratitude to my FYP supervisor, Dr. Azmi Bin Abdul Wahab for giving an opportunity to me to learn throughout this project. Again, I would like to extend my thanks and deep appreciation to him, whose guidance and advice had helped me a great deal in completing this project.

I also gratefully acknowledged the assistance and guidance from: (1) Mr. Andy (Schmidt + Clemens); (2) Mr. Anuar (UTP Technician); (2) Mr. Faisal (UTP Technician); (3) Mr. Irwan (UTP Technician).

I would also like to express my greatest gratitude towards my family and friends who believed in me and constantly supported the work throughout the two semesters. Finally, I appreciate for those whose names were not included who either directly or indirectly helped me to complete this project.

TABLE OF CONTENT

CERTIFICATION OF APPROVAL.	ii
CERTIFICATION OF ORIGINALITY.	iii
ABSTRACT.	iv
ACKNOWLEDGEMENT	vi
CHAPTER 1: INTRODUCTION	1
1.1 Background of Study	1
1.1 Problem Statement	1
1.2 Objectives.	2
1.3 Scope of Study.	3
CHAPTER 2: LITERATURE REVIEW	4
2.1 Microstructure Characterization	4
2.2 Stainless Steel	7
2.2.1 Types of Stainless Steel	7
2.3 Reformer Tube	10
2.3.1 Reformer Tube in Operation	10
2.3.2 Centrifugally Cast Reformer Tube	11
2.4 Creep	14

CHAPTER 3:	METHODOLOGY	16
3.1	Methodology	16
3.2	Sample Preparation	17
3.2.1	Sectioning	17
3.2.2	Mounting	18
3.2.3	Grinding and Polishing	19
3.2.4	Etching	20
3.3	Image Capturing	21
3.4	Data Analysis	21
CHAPTER 4:	RESULTS AND DISCUSSION	26
CHAPTER 5:	CONCLUSION AND RECOMMENDATION	36
REFERENCES	39
APPENDICES	42

LIST OF FIGURES

Figure 2.1	Reformer tubes	10
Figure 2.2	Centrifugal casting	11
Figure 2.3	Creep curve strain against time	15
Figure 3.1	Methods involved in the project	16
Figure 3.2	Creep-tested samples that have been sectioned	17
Figure 3.3	Hot mounting equipment and mounted samples	19
Figure 3.4	Grinding and polishing equipment	19
Figure 3.5	BSE image of the microstructure	23
Figure 3.6	Cropped image from the BSE image	23
Figure 3.7	Threshold Cr image of the cropped image from BSE image	24
Figure 3.8	Outlined numbered threshold image, results and summary	25
Figure 4.1	Microstructure of as-cast material	26
Figure 4.2	Spectra obtained by SEM with spot mode	28
Figure 4.3	Microstructure of creep-tested material	29
Figure 4.4	OM image showing void	31
Figure 4.5	OM image of voids in creep-tested samples	32
Figure 4.6	BSE image showing void locations	33

Figure 4.7	Graph of average particle size and percentage area of Cr and Nb	35
Figure A-1	BSE image of creep-tested sample loaded by NIH Image J	43
Figure A-2	Measuring length of scale (bottom left corner)	43
Figure A-3	Clicking at “Image” toolbar	44
Figure A-4	Clicking at “Properties”	44
Figure A-5	Converting from pixel to unit of length	45
Figure A-6	Inputting the conversion factor into pop up window	45
Figure A-7	Cropping a portion of the BSE image	46
Figure A-8	Clicking at “Image” toolbar	46
Figure A-9	Clicking at “Crop”	47
Figure A-10	Cropped BSE image to measure Cr	47
Figure A-11	Clicking at “Image” toolbar	48
Figure A-12	Clicking at “Adjust”	48
Figure A-13	Clicking at “Threshold”	49
Figure A-14	Adjusting “Threshold” limits to show only Cr	49
Figure A-15	Cr image (black) only appeared at pop out window	50
Figure A-16	Clicking at “Analyze”	50
Figure A-17	Clicking at “Analyze Particle”	51
Figure A-18	“Analyze Particle” pop up window	51

Figure A-19 Changing the “show” input box from “Nothing” to “Outlines”	52
Figure A-20 Result (1-28) of cropped Cr image	52
Figure A-21 Result (29-59), of cropped Cr Image	53
Figure A-22 Cropped BSE image to measure Nb	54
Figure A-23 Clicking at “Image” toolbar	54
Figure A-24 Clicking at “Adjust”	55
Figure A-25 Clicking at “Threshold”	55
Figure A-26 Adjusting “Threshold” limits to show only Nb	56
Figure A-27 Nb image (black) only appeared at pop out window	56
Figure A-28 Clicking at “Analyze” toolbar	57
Figure A-29 Clicking at “Analyze Particles”	57
Figure A-30 Changing the “show” input box from “Nothing” to “Outlines”	58
Figure A-31 Result (1-28) of cropped Nb image	58
Figure B-1 Average particle size of Cr and Nb	62
Figure B-2 Percentage area of Cr and Nb	62
Figure C-1 Periodic table	64
Figure C-2 Periodic table showing increasing radius direction	65
Figure C-3 Periodic table showing increasing ionization energy direction	65

LIST OF TABLES

Table 3.1	SiC grit size and wheel speed for grinding	20
Table 3.2	Etchants used on the Austenitic Stainless Steel	21
Table 4.1	Measurement compared between NIH ImageJ and Intercept method	34
Table 4.2	Average particle size and percentage area of as-cast and creep- tested samples	35
Table B-1	Average particle size and percentage area of creep-tested sample 321 measured by using the intercept method	60
Table B-2	Average particle size and percentage area of the as-cast sample	60
Table B-3	Average particle size and percentage area of sample 320	60
Table B-4	Average particle size and percentage area of sample 321	61
Table B-5	Average particle size and percentage area of sample 322	61
Table B-6	Average particle size and percentage area of sample 326	61
Table C-1	Elements, percent weight and percent atomic in as-cast Nb-rich precipitate obtained by spot mode	64
Table C-2	Elements, percent weight and percent atomic in creep-tested sample 321, Nb-rich precipitate by spot mode	64

LIST OF APPENDIX

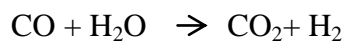
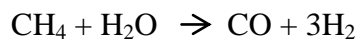
APPENDIX A	Using NIH ImageJ	42
APPENDIX B	Results	59
APPENDIX C	Conclusion	63

CHAPTER 1

INTRODUCTION

1.1 Background and Problem Statement

In petrochemical plants, the production of hydrogen from natural gas is carried out in steam methane reformers also known as hydrogen reformers, where the following reactions occur in the presence of a nickel catalyst:



Reformer tubes are vertically oriented straight tubes referred to as catalyst tubes. During plant operation the tubes are filled with catalyst while gasses pass through the catalyst at extremely high temperatures of more than 900°C and internal pressure of approximately 2MPa. The tube material in the catalyst tubes is susceptible to a failure mechanism referred to as "creep". Creep occurs due to the harsh environment to which the tubes are exposed, including elevated temperatures and mechanical loading cycles as its expected service requirements of usually more than 100,000 hours (11.4 years).

Before the reformer tubes can be used at high temperature, they have to undergo creep testing procedures. Several samples of the creep-tested reformer tubes have been obtained and their microstructures have not yet been characterized. In order to fully understand the material behavior under creep we need to also characterize the microstructure of the creep-tested samples.

In recent years, the experimental procedures for characterizing the microstructure, including phase identification, the morphology of primary and secondary precipitates, as well as studies of phase transformation, have been well developed and reported in the literature. However, a review of the results contained in more recently published papers dealing with reformer tube material indicate that these characterization techniques should be discussed more fully in order to clarify their capabilities for the identification of phases and transformation mechanisms, and also to show how they contribute to an understanding of the role of additive elements in developing improved mechanical properties (Almeida, et. al., 2003).

In this project, five samples of a centrifugally-cast austenitic stainless steel of reformer tube have been characterized by different techniques. These techniques are described and their application to phase identification is illustrated.

1.2 Objectives

The project is conducted to study the effect of creep in reformer tube material by comparing the microstructures in the as-cast material with the creep-tested material.

Targeted reformer tube life is about 100,000 hours. Strength and performance of the reformer tube is usually based on 1,000 hours of creep test. When comparing to 1,000 hours of creep test with 100,000 hours of actual service life of the reformer tube, the microstructure of the more rapid “ageing” process during creep tests may not be similar to microstructure obtained from actual reformer tubes in service.

The main objective in this project is to identify the precipitates that exist in both the as-cast and creep-tested material and to study the transformation of this microstructure in terms of shape, average particle size, percentage particle area and additional microstructure formed when compared to the microstructure in the as-cast material. Future work will study the precipitates that exist in ex-service reformer tubes.

1.3 Scope of study

This project is limited to one type of reformer tube material which is the Schmidt + Clemens CA4852 micro alloy. The creep-tested samples were obtained from Schmidt and Clemens in Spain. These samples had already been creep-tested by Schmidt + Clemens (Spain). The as-cast sample was also provided from the same reformer tube for comparison. This study also was concentrated only on one type of alloy although there are many other types of alloys being used to manufacture reformer tubes. The work done in this project was only one part of the bigger picture that could represent the behavior and effect of creep to the reformer tube.

CHAPTER 2

LITERATURE REVIEW

2.1 MICROSTRUCTURE CHARACTERIZATION

Microstructure characterization is important because it gives an insight about the identification of phases and transformation mechanisms and to show the role of how additive elements can contribute in developing improved mechanical properties (Almeida, et. al., 2003). There are various numbers of research and studies that have been carried out which is related to the microstructure characterization. Each of the studies has different work scopes depending on the objectives.

Before microstructure can be characterized, the required metals had to be prepared. That is when metallography comes into play. The primary objective of metallographic preparation is to reveal the constituents and structure of metals and their alloys by means of sampling, sectioning, mounting, grinding, polishing and etching. When sampling, the specimens selected for preparation must be representative of the material to be examined. This is to ensure that the test sample taken from the parent sample would give as much information with respect to purpose of the study. Sectioning is to break the large samples from sampling into small sizes of samples. Generally the size of the sectioned samples should be not more than about 12 to 25 mm (0.5 to 1.0 in) square, or approximately 12 to 25 mm in diameter if the material is round. The height of the sectioned samples should be no greater than necessary for convenient handling during grinding and polishing. The main purpose of mounting the samples is for convenience in handling specimens of difficult shape and sizes during the subsequent steps of

metallographic preparation and also for edge preservations by means of mechanical mounting or plastic mounting. Grinding is to remove the deformation region induced by the sectioning process by pressing the sample on a rotating piece of abrasive papers, using water to wash away grinding debris and also to act as a lubricant. Grinding should start with the coarser paper to the finest paper to produce a flat surface. After grinding, polishing is the final step in producing a deformation-free surface that is flat, scratch free and mirror-like in appearance. Polishing usually is conducted with 6- or 3- μm diamond abrasives charged onto polishing cloths. Finally, etching is done to further reveal structural aspects such as porosity, cracks, nonmetallic inclusions and structural details of the samples by immersion or swabbing with a suitable chemical solution that essentially attack the surface of the metal (Leco, 2002).

Microstructure characterization is done after the sample have been prepared. The optical microscope (OM) often referred to as “light optical microscope”, is a type of microscope which uses visible light and a system of lenses to magnify images of small samples. Optical microscope usually is equipped with various video cameras allowing the images to be displayed on high resolution video monitors. But usable magnification of the optical microscope is limited to only up to 1000 times. Therefore scanning electron microscope (SEM) can be used to further increase the magnification to further characterize the microstructure. Scanning electron microscope images the sample surface by scanning it with a high-energy beam of electrons. The electrons interact with the atoms that make up the sample by producing signals that contain information about the sample. Electronic devices are used to detect and amplify the signals and display them as an image on a cathode ray tube. The image may be photographed from a high resolution cathode ray tube, but in modern machines is digitally captured and displayed on a computer monitor. The types of signals made by SEM can include secondary electrons, backscattered electrons and characteristic x-rays. These signals come from the beam of electrons striking the surface of the specimen and interacting with the sample at or near its surface. In its primary detection mode, secondary electron imaging, the SEM can produce very high-resolution images of a sample surface, revealing details about 1 to 5 nm in size. Due to the way these images are created, SEM micrographs

have a very large depth of focus yielding a characteristic three-dimensional appearance useful for understanding the surface structure of a sample. This great depth of field and the wide range of magnifications (commonly from about 25 times to 250,000 times) are available in the most common imaging mode for specimens in the SEM. Characteristic x-rays are the second most common imaging mode for an SEM. X-rays are emitted when the electron beam removes an inner shell electron from the sample, causing a higher energy electron to fill the shell and give off energy. These characteristic x-rays are used to identify the elemental composition of the sample. Back-scattered electrons (BSE) that come from the sample may also be used to form an image. Back-scattered electrons images are often used in analytical SEM along with the spectra made from the characteristic x-rays as clues to the elemental composition of the sample. The SEM can also be used to form electron backscatter diffraction (EBSD) image. This image can be used to determine the crystallographic structure of the sample. Transmission electron microscope (TEM) can also be used to characterize fine intragranular precipitates present in the sample (Wikipedia, 2008).

Characterization of the microstructure is important for several form of analyze:

- (i) To determine the aging in a cast heat resisting alloy (Rodriguez, et. al., 2000)
- (ii) 3D analysis of creep voids in hydrogen reformer tubes (Abdul Wahab, Kral, 2005).
- (iii) Determining the effects of the addition of the modifying elements to increase the creep resistance (Soares, Almeida, 1992).

Therefore, microstructure characterization should be considered as integral to help fulfill the goals of various studies.

2.2 STAINLESS STEEL

In metallurgy, stainless steel is defined as an iron-carbon alloy with a minimum of 11.5 wt% chromium content. Stainless steel does not stain, corrode or rust as easily as ordinary steel (it "stains less"), but it is not stain-proof. It is also called corrosion resistant steel when the alloy type and grade are not detailed, particularly in the aviation industry. There are different grades and surface finishes of stainless steel to suit the environment to which the material will be subjected in its lifetime (Wikipedia, 2008).

High oxidation-resistance in air at ambient temperature is normally achieved with additions of a minimum of 13% (by weight) chromium, and up to 26% is used for harsh environments. The chromium forms a passivation layer of chromium (III) oxide (Cr_2O_3) when exposed to oxygen. The layer is too thin to be visible, which means that the metal remains lustrous. It is, however, impervious to water and air, protecting the metal beneath. Also, this layer quickly reforms when the surface is scratched. This phenomenon is called passivation and is seen in other metals, such as aluminium and titanium. When stainless steel parts such as nuts and bolts are forced together, the oxide layer can be scraped off causing the parts to weld together. When disassembled, the welded material may be torn and pitted, an effect that is known as galling. This destructive galling can be best avoided by the use of dissimilar materials, e.g. bronze to stainless steel, or even different types of stainless steels (martensitic against austenitic, etc.), when metal-to-metal wear is a concern. In addition, Nitronic alloys (trademark of Armco, Inc.) reduce the tendency to gall through selective alloying with manganese and nitrogen. Nickel also contributes to passivation, as do other less commonly used ingredients such as molybdenum and vanadium (Wikipedia, 2008).

2.2.1 Types of Stainless Steel

There are different types of stainless steels: when nickel is added, for instance, the austenite structure of iron is stabilized. This crystal structure makes such steels non-magnetic and less brittle at low temperatures. For higher hardness and strength, carbon is added. When subjected to adequate heat treatment, these steels are used as razor

blades and cutleries. Significant quantities of manganese have been used in many stainless steel compositions. Manganese preserves an austenitic structure in the steel as does as nickel, but at a lower cost. Stainless steels are also classified by their crystalline structure:

- Austenitic or 300 series, stainless steels comprise over 70% of total stainless steel production. They contain a maximum of 0.15% carbon, a minimum of 16% chromium and sufficient nickel and/or manganese to retain an austenitic structure at all temperatures from the cryogenic region to the melting point of the alloy. A typical composition of 18% chromium and 10% nickel, commonly known as 18/10 stainless, is often used in flatware. Similarly, 18/0 and 18/8 are also available. Super-austenitic stainless steels, such as alloy AL-6XN and 254SMO, exhibit great resistance to chloride pitting and crevice corrosion due to high molybdenum contents (>6%) and nitrogen additions, and the higher nickel content ensures better resistance to stress-corrosion cracking over the 300 series. The higher alloy content of super-austenitic steels makes them more expensive.
- Ferritic stainless steels are highly corrosion-resistant, but less durable than austenitic grades. They contain between 10.5% and 27% chromium and very little nickel, if any. Most compositions include molybdenum; some, aluminium or titanium. Common ferritic grades include 18Cr-2Mo, 26Cr-1Mo, 29Cr-4Mo, and 29Cr-4Mo-2Ni.
- Martensitic stainless steels are not as corrosion-resistant as the other two classes but are extremely strong and tough, as well as highly machineable, and can be hardened by heat treatment. Martensitic stainless steel contains chromium (12-14%), molybdenum (0.2-1%), nickel (0-<2%), and carbon (about 0.1-1%) (giving it more hardness but making the material a bit more brittle). It is quenched hardened and magnetic. It is also known as series-00 steel.

- Precipitation-hardening martensitic stainless steels have corrosion resistance comparable to austenitic varieties, but can be precipitation hardened to even higher strengths than the other martensitic grades. The most common, 17-4PH, uses about 17% chromium and 4% nickel. There is a rising trend in defense budgets to opt for an ultra-high-strength stainless steel if possible in new projects, as it is estimated that 2% of the U.S. GDP is spent dealing with corrosion. The Lockheed-Martin Joint Strike Fighter is the first aircraft to use a precipitation-hardenable stainless steel—Carpenter Custom 465—in its airframe.
- Duplex stainless steels have a mixed microstructure of austenite and ferrite, the aim being to produce a 50/50 mix, although in commercial alloys, the mix may be 40/60 respectively. Duplex steels have improved strength over austenitic stainless steels and also improved resistance to localised corrosion, particularly pitting, crevice corrosion and stress corrosion cracking. They are characterised by high chromium (19–28%) and molybdenum (up to 5%) and lower nickel contents than austenitic stainless steels.
- Cast steel of 25% Cr – 20% type (HK type steel) had been used since 1960s. It had been used for high temperature environments such as in reformer furnaces. This class of steel had replaced the traditional superalloys with a reduction in costs and has similar properties under condition of creep. Ni content if increased to around 35% will produce HP type steels.

2.3 REFORMER TUBE

Reformer tubes (Figure 2.1) can be found in hydrogen, ammonia, and methanol process plants around the world. Typically, reformer tubes contain several hundred vertically orientated straight tubes, referred to as catalyst tubes. The Inner Diameter (ID) of these particular tubes is generally between 76.2 mm (3.0 inches) and 127 mm (5.0 inches) (Abdul Wahab, Kral, 2005).



Figure 2.1: Reformer tubes

2.3.1 Reformer Tube in Operation

Reformer tubes do not have an infinite life and usually they are given a nominal service life of approximately 100,000 hours (approximately 12 years) after which it is estimated the creep damage is too severe to continue to service. At about this 100,000 hour point, they are usually removed from service and replaced.

Reformer tubes have a very important role to play in the petrochemical industry and they can be represented by the amount of capital cost involved. For instance, the purchase of a single tube is approximately US\$7,000 with a complete change costing around US\$8 millions for one plant. Meanwhile, a prematurely failed tube forces the

shutdown of the plant and it may take about 7 days to be replaced and may cost between US\$0.5 to US\$ 1.5 million in lost profit. Therefore, being able to identify and locate such damage in its early stages of growth is essential for safe and low running cost plant operation. Thus, sometimes a small number of the tubes are sectioned and analyzed to determine the true extent of the creep damage.

2.3.2 Centrifugally Cast Steel Reformer Tubes

Figure 2.2 shows a typical centrifugal casting process. The essential feature of centrifugal casting is the introduction of molten metal into a mould which is rotated during solidification of the casting. The centrifugal force thus plays an important role in shaping and in feeding according to the variation of the process employed. The casting of a plain pipe or tube is accomplished by rotation of a mould about its own axis, the bore shape being produced by centrifugal force alone and the wall thickness determined by the volume of metal introduced. This practice is widely referred to as true centrifugal casting. One of its most popular applications in the manufacturing industry is to produce reformer tubes because of the advantages of the process for its suitability for casting cylindrical forms and produce high metallurgical quality of the product (Campbell, 1991).

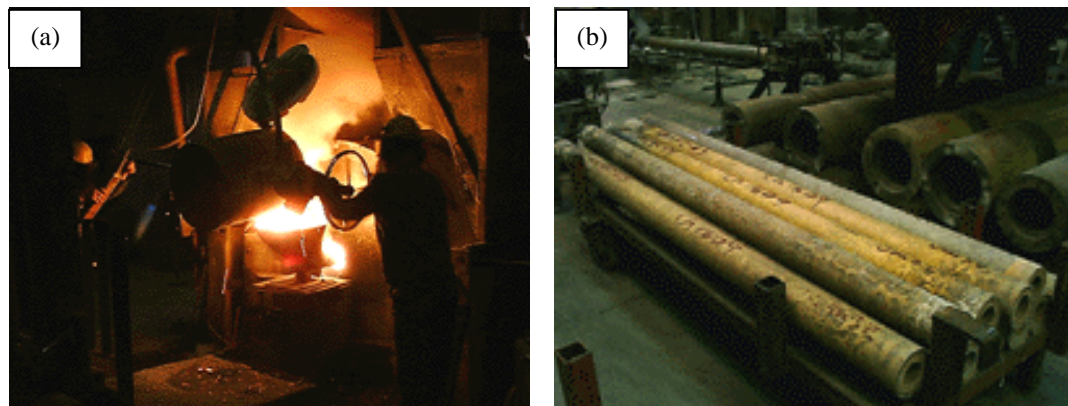


Figure 2.2: Centrifugal casting: (a) Molten metal is poured into the rotating machine; (b) tubes produced.

The petrochemical industry has been using cast steel of the 25% Cr–20% Ni type (HK type steel) since the early 1960s in reformer and pyrolysis furnaces. This class of steel had replaced the traditional superalloys with a reduction in costs and has similar properties under conditions of creep, which is one of the principal degradation mechanisms leading to failure in service at elevated temperature (Almeida, et. al., 2003).

It is designed to sustain operation while exposed to operating temperatures in excess of 650°C. These materials are made primarily from iron, chromium, and nickel; niobium, titanium, vanadium, or zirconium are common additions to provide for higher creep resistance, as they are able to form dispersed phases stable at the working temperature. These materials are commonly used in a commercial manner in gas turbines, metal treatment equipment, reformer furnaces, etc., where they may be subjected to oxidizing, sulfidizing, or carburizing environments (Rodriguez, et. al., 2000).

The as-cast microstructure of alloys with high chromium and nickel contents consists of an austenite matrix and a network of primary carbides; ferrite can be encountered in alloys with low nickel and high chromium contents. Exposure at the service temperature may promote the dissolution of primary carbides and development of a fine array of secondary carbides precipitated from the highly supersaturated matrix. These secondary carbides may be able to coarsen as time at the service temperature lengthens (Rodriguez, et. al., 2000).

Centrifugally cast austenitic stainless steel alloys containing high amounts of carbon (0.4 wt. %), chromium (25 wt. %) and nickel (20–35 wt. %) were developed for these purposes. The additions of Cr and Ni are well known for improving corrosion resistance and strength at elevated temperatures, while the high amount of C inhibits brittle σ -phase formation (Rodriguez, et. al., 2000).

Creep strengthening is achieved via the formation of Cr-rich $M_{23}C_6$ carbides in the reformer tube microstructure. Primary carbides, which form a grain boundary network during casting, are suspected to play an important role in restraining grain boundary

sliding. The secondary carbides, which appear as fine intragranular precipitates during service, are believed to hinder dislocation motion. With increasing service time, the primary and secondary Cr-rich $M_{23}C_6$ carbide particles have a tendency to coarsen, which in turn reduces creep strength. Additions of Nb and Ti lead to “fragmentation” and refinement of the grain boundary carbide network, as well as creating a finer and more stable dispersion of intergranular carbides, which would all result in added creep resistance (Abdul Wahab, Kral, 2005)

The use of the centrifugal casting technique for tube production has also contributed to higher performance of these components. Better creep properties have been attributed to the morphological modifications introduced in the microstructure and to the presence of more stable phases during aging while in long-term service. The base composition has also been adjusted with increase in the Ni content to around 35% to produce the HP type steels. The addition of niobium, and more recently niobium-plus-titanium, has promoted the fragmentation of the as-cast microstructure and the partial replacement of chromium carbides by more stable ones. Other elements such as molybdenum, zirconium, and vanadium have been introduced to the chemical composition of these steels with similar effects. The addition of rare-earth elements has also been considered. The creep resistance of these alloys is dependent on the chemical composition and on the distribution of the phases that form during casting or that transforms within them during service. The primary eutectic-like carbide network appears to play an important role in preventing grain boundary sliding. Secondary precipitation in the form of a fine distribution of cube-shaped chromium carbides should act to restrict the motion of dislocations (Abdul Wahab, Kral, 2005).

Studies in the past have attempted to relate creep with the microstructure changes and in particular to investigate the circumstances surrounding the formation of creep voids. The changes in properties exhibited by HP steels on ageing as a function of the duration of service are well known empirically, but very little information can be related for the reasons for the changes. Therefore the phases present in the as-cast and the aged samples should be studied for comparison (Borges, 1999).

Similar approach had also been taken in other related work to characterize the microstructure of the centrifugally cast steel furnace tubes and the importance of the addition of modifying elements such as titanium, niobium and chromium. A complete description of the phases present in the as-cast, welded and aged condition was made as a function of the modifying elements. The microstructure of primary carbides, secondary precipitation, niobium carbide instability at elevated temperatures and the effect of titanium on the reaction were discussed. It was indicated that partial transformation and the effect of titanium was one of the explanations for the superior creep properties observed in the centrifugally cast steel furnace tubes materials. It was concluded that the niobium concentration and the presence of titanium as a modifier element in HP-modified steels determine the micro-structural morphology in the as-cast and aged conditions. The concentration of Niobium promotes the primary “Chinese script” morphology and titanium promotes a finer and more distributed secondary precipitation. A finer and more evenly distributed secondary precipitation, a less continuous dendritic carbide network and smaller volume fraction transformed to G-phase observed in the alloy modified with titanium may be the explanation for the superior creep properties observed in the steel with the addition of titanium compared with only having the addition of niobium alone (Almeida, et. al., 2003).

Strengthening mechanisms were also looked at to improve the resistance of reformer tubes from creep failure not only on the effect of the addition of modifier elements such as niobium and more recently niobium-plus-titanium, molybdenum, zirconium, vanadium and rare-earth elements to replace partially chromium carbides (Almeida, et. al., 2003). Also the usage of the centrifugal casting technique for tube production also has contributed to the increase in performance and resistance from creep failures (Wu, et.al, 2000).

2.4 CREEP

Creep is the term used to describe the tendency of a ‘solid’ material to slowly move or deforms permanently to relieve stresses. It occurs as a result of long term exposure to levels of stress that are below the yield strength or ultimate strength of the material.

Creep is more severe in materials that are subjected to heat for long periods, and near the melting point. It is often observed in glasses (Callister, 2003).

The rate of this deformation is a function of the material properties, exposure time, exposure temperature and the applied stress. Depending on the magnitude of the applied stress and its duration, the deformation may become so large that a component can no longer perform its function - for example creep of a turbine blade will cause the blade to contact the casing, resulting in the failure of the blade. Creep is usually of concern to engineers and metallurgists when evaluating components that operate under high stresses or high temperatures. Creep is not necessarily a failure mode, but is instead a deformation mechanism. Moderate creep in concrete is sometimes welcomed because it relieves tensile stresses that otherwise may have led to cracking (Callister, 2003).

Creep behavior is usually presented as a creep curve in the form of strain versus time graph as in Figure 2.3. From Figure 2.3, there are three distinct creep stages called transient creep, steady-state creep and accelerating creep. Transient creep or type I or primary creep consists of an initially high strain rate which soon decreases to the constant rate found in the type II or secondary creep also known as the steady state creep. In this region, creep remains constant until it enters into type III or tertiary creep region when the strain rate in this region increases with respect to time until failure (Callister, 2003).

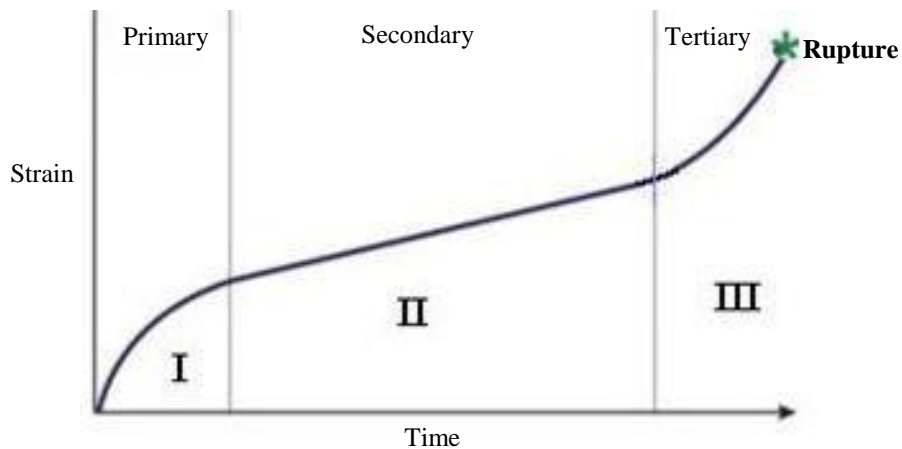


Figure 2.3: Creep curve of strain vs time

CHAPTER 3

METHODOLOGY

3.1 METHODOLOGY

Figure 3.1 shows the overall methods applied in this project. Sample preparation stage contains sectioning, mounting, grinding, polishing and etching processes. Microstructure observation and image capturing were performed by using OM and SEM. Finally, characterization and data analysis were done by using open sourced software called NIH ImageJ.

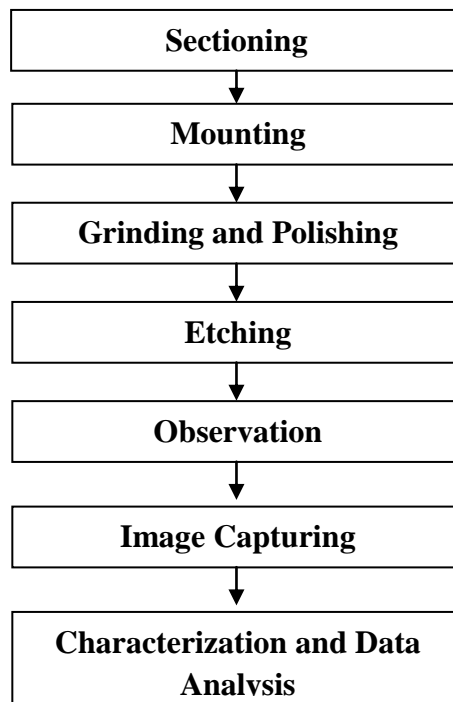


Figure 3.1: Methods involved in the project

3.2 SAMPLE PREPARATION

The samples were prepared in order to produce a mirror like surface to analyze the microstructures of the materials. The sample preparation consists of few methods which would be discussed further in this chapter.

All preparation methods were referred to the ASTM Standards Volume 3.01 designated in section E3-95 titled Standard Practice for Preparation of Metallographic Specimens (Dreyfuss, 2004).

3.2.1 Sectioning

Sectioning is the removal of a representative sample from the parent piece by removing a suitably sized specimen from the larger mass at the desired location and orientation. The sectioning plane should be as near to the desired location as possible. The microstructure must not be altered in the process. High speed abrasive sectioning or low speed low deformation precision sectioning can be used.

Figure 3.2 shows the creep-tested samples that had been sectioned. In this project, all the samples obtained had already been sectioned in the longitudinal plane of the parent sample. The average length of each sectioned sample was 13 mm.



Figure 3.2: Creep-tested samples that have been sectioned; (a) Sample 320; (b) Sample 321; (c) Sample 322; (d) Sample 326.

3.2.2 Mounting

The primary purpose of mounting metallographic specimens is for convenience in handling specimens of difficult shapes or sizes during the subsequent steps of metallographic preparation and examination. A secondary purpose is to protect and preserve extreme edges or surfaces defects during metallographic preparation. Usually there are of two types of mounting methods that can be applied that is cold or hot mounting. Cold mounting is performed with a mixture of resin and hardener but hot mounting uses a certain amount of pressure and heat to mount the samples.

Figure 3.3a shows the hot mounting equipment, while Figure 3.3b is the mounted samples in Bakelite powder. In this project, hot mounting was applied and it would not affect the microstructures of the samples because the range of the temperature of the mounting process is from 140°C to 160°C (Dreyfuss, 2004) that is only a fraction of the reformer tube operating temperature of 800°C to 900°C. Below is listed the hot mounting equipment's parameters:

- Equipment: SIMPLIMENT 1000, AUTOMATIC MOUNTING PRESS
- Powder: Bakelite green or black powder
- Heat time: 2 minutes
- Cool time: 5 minutes
- Temperature: 140°C to 160°C
- Pressure: 4200 psi

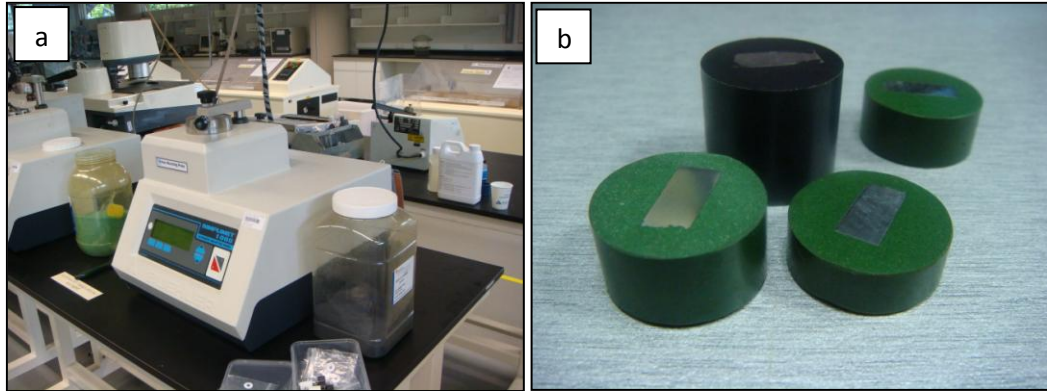


Figure 3.3: (a) Hot mounting equipment; (b) mounted samples

3.2.3 Grinding and Polishing

Figure 3.4 shows the grinding and polishing equipment. Grinding can be divided into two parts. Coarse grinding produce an initial flat surface and fine grinding remove the zone of deformation due to sectioning and coarse grinding. The depths of deformation during the grinding and polishing stage can be limited by proper abrasive size sequencing. All grinding steps were performed with water as the lubricant. Water also minimized specimen heating and prevented the abrasive from becoming loaded with metal removed from the specimen being prepared.



Figure 3.4: Grinding and polishing equipment

Polishing was the final step in producing a deformation-free surface that is flat, scratch free and mirror like in appearance. This is to observe the true microstructure for subsequent metallographic interpretation, both qualitative and quantitative. Polishing can be divided into two parts. Rough polishing is a further limitation of the deformation zone produced by fine grinding and final polishing is to remove the deformation zone produced during rough polishing.

The samples underwent grinding and polishing steps as shown in the Table 3.1. It was done with 6 and 3 μ m diamond paste charged onto a low nap cloth. A control sample was also prepared from an as-cast tube made from the same alloy to compare the microstructures with the microstructures of the creep-tested samples.

Table 3.1: SiC grit size and wheel speed for grinding

SiC Grit Size	Wheel Speed (RPM)
120	150
320	150
400	150
600	150
800	150
1200	150

3.2.4 Etching

All preparation and etching processes were referred from the ASTM Standards Volume 3.01 designated in section E381-94 titled Standard Method of Macroetching and E407-99 titled Standard Practice for Microetching Metals and Alloys (Dreyfuss, 2004). Etching is the process to reveal structural details by preferential attack of a metal surface with an acid or basic chemical solution to reveal inclusions, porosity, cracks, intergranular corrosion and structural details of the samples.

The samples were etched in glyceresia. Table 3.2 shows the glyceresia composition, reaction type and methods applied in this project. However, glyceresia could not be stored for a period of time due to the degradation over time and there is also a potential of changing into nitro-glycerin over time.

Table 3.2: Etchants used on the Austenitic Stainless Steel

	Composition	Type	Method
Glyceresia	10ml Glycerol, 15ml HCl, 5ml HNO ₃	Delineating	Swab or immerse from 30-60secs

3.3 IMAGE CAPTURING

A number of different micrographs were obtained at different range of magnification by using optical microscope at magnifications of 50X, 100X and 200X. Each micrograph of the samples was taken from 4 different locations by using a Nikon ECLIPSE ME600 with JVC colour video camera with bright-field and ND filters.

Scanning electron microscope (SEM) with secondary electron (SE) and back scattered electron (QBSD) imaging was also used in this project. The equipment employed for SEM and QBSD is LEO 1430 VP SEM. The samples were coated before inserted into the SEM. Energy Dispersive Spectroscopy (EDS) by spot mode was also used to confirm the precipitates present in the material.

3.4 DATA ANALYSIS

NIH ImageJ is a public domain Java image processing program inspired by NIH Image for the Macintosh. It runs, either as an online applet or as a downloadable application, on any computer with a Java 1.4 or later virtual machine. Downloadable distributions are available for Windows, Mac OS, Mac OS X and Linux. It can display, edit, analyze, process, save and print 8-bit, 16-bit and 32-bit images. It can read many image formats

including TIFF, GIF, JPEG, BMP, DICOM, FITS and "raw". It supports "stacks", a series of images that share a single window. It is multithreaded, so time-consuming operations such as image file reading can be performed in parallel with other operations. It can calculate area and pixel value statistics of user-defined selections. It can measure distances and angles. It can create density histograms and line profile plots. It supports standard image processing functions such as contrast manipulation, sharpening, smoothing, edge detection and median filtering. It does geometric transformations such as scaling, rotation and flips. The image can be zoomed up to 32:1 and down to 1:32. All analysis and processing functions are available at any magnification factor. The program supports any number of windows (images) simultaneously, limited only by available memory. Spatial calibration is available to provide real world dimensional measurements in units such as millimeters. Density or gray scale calibration is also available. NIH ImageJ was designed with an open architecture that provides extensibility via Java plugins. Custom acquisition, analysis and processing plug ins can be developed using NIH ImageJ's built in editor and Java compiler. User-written plugins make it possible to solve almost any image processing or analysis problem and the plugins code is freely available (Rasband, 2008).

In this project (see Appendix A), NIH ImageJ was used to measure the average particle size and percentage area of each particle. This technique was chosen instead of the manual method specified by the ASTM standards because of its better accuracy and repeatability. In addition, the ASTM method is much slower and is rather difficult to perform. The next paragraphs illustrate the calculation of the average particle size and percentage area of Cr. All the methods described in these paragraphs are applied in the same manner to calculate the average particle size and percentage are of Nb.

Figure 3.5 shows the BSE image of the microstructure of the creep-tested sample 321 loaded by ImageJ. For ease in measuring the average particle size and percentage area of each particle, the image had to be cropped into small sections of images in order to not complicate the measuring process. Figure 3.6 shows the cropped image from the BSE image of the microstructure of the creep-tested sample of 321 (Figure 3.5).

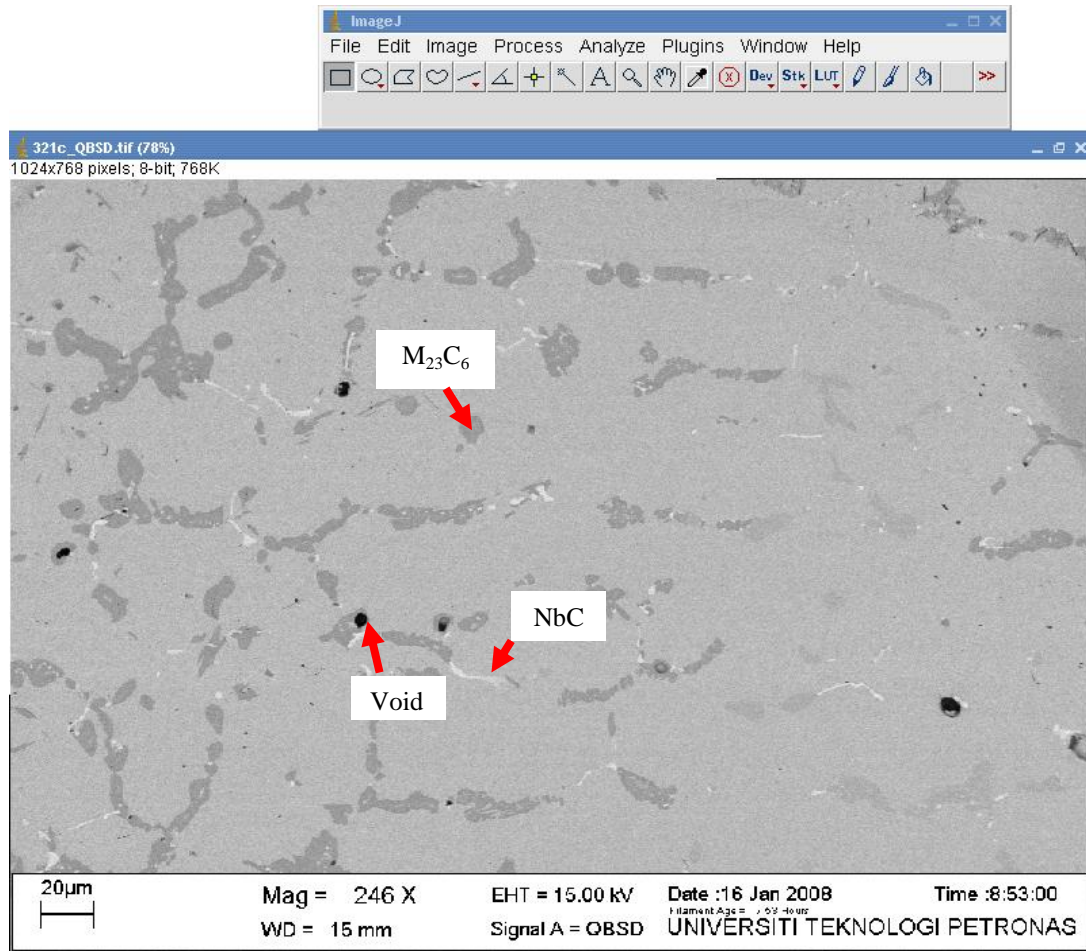


Figure 3.5: BSE image of the microstructure of the creep-tested sample 321.

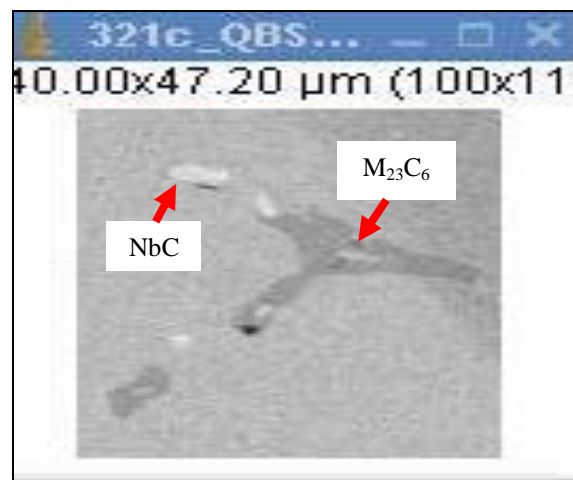


Figure 3.6: Cropped image from the BSE image of the microstructure of the creep-tested sample of 321.

After cropping, the image had to be thresholded to invert the cropped image (Figure 3.6) into a black and white image as shown in Figure 3.7. To calculate the average particle size and percentage area of Cr, Figure 3.6 was threshold so that Cr became black and Nb turned into white so that only Cr appeared in the pop out window (Figure 3.7). This was to ensure that only Cr was measured by NIH ImageJ.

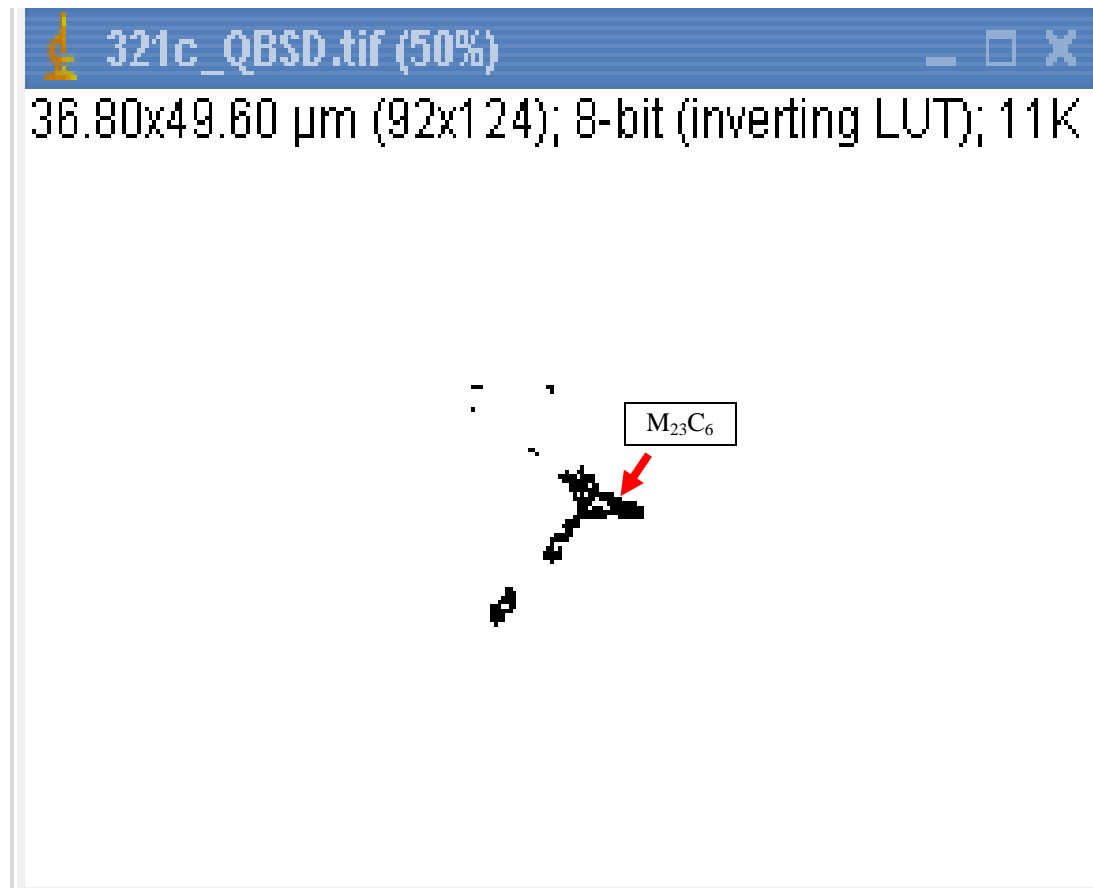


Figure 3.7: Thresholded Cr image of the cropped image from the BSE image of the microstructure of the creep-tested sample 321.

After the image had been thresholded, the Cr particle was analyzed. This command counts and measures the thresholded image by scanning the selected particle until it finds the edges of the particle to complete an outline. The average particle size was measured based on the outline. Figure 3.8 shows the numbered outline of the particle,

results and summary of the particle size. The results will then be tabulated in the spreadsheet.

The values obtained from NIH ImageJ were also compared with the ASTM Standard method to compare and determine the accuracy of the average particle size and percentage area. A transparency marked with small boxes of 1 by 1 cm was used as a tracing medium, was traced onto the BSE image and the area of the particle that lied in the 1 by 1 cm box was calculated and then converted into the image's scale.

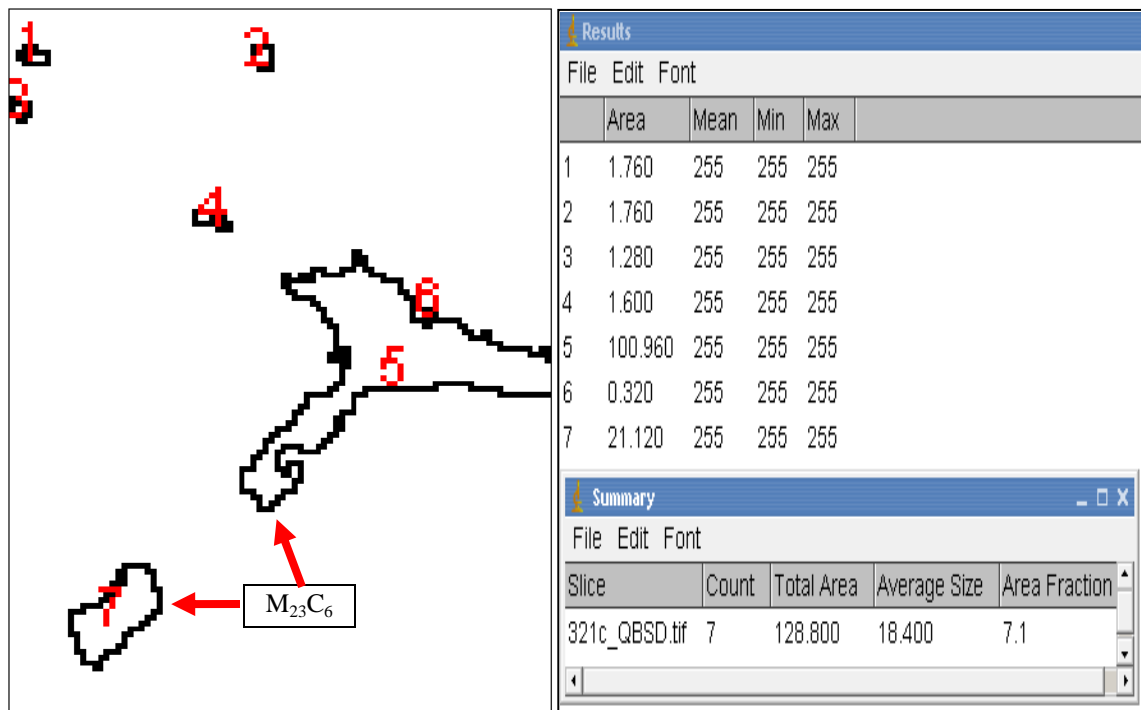
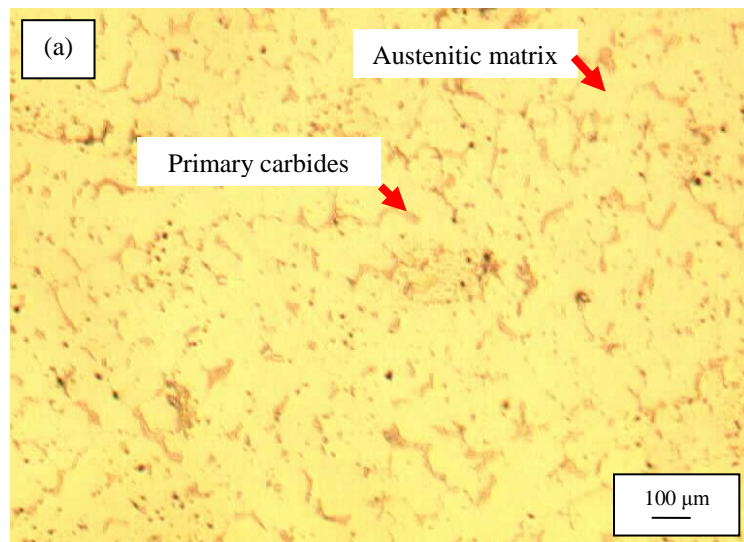


Figure 3.8: Outline numbered threshold image, results and summary of the results by the particle analyzer.

CHAPTER 4

RESULT AND DISCUSSION

Figure 4.1 shows the microstructure of the as-cast material. The optical image (Figure 4.1a) shows the austenitic matrix (light coloured area) with a network of primary carbides (slightly darker area). The image obtained from the secondary electrons (Figure 4.1b) does not provide sufficient information about the types of carbides appeared in the material but the image taken from the BSE image (Figure 4.1c), shows that the network is made of two different types of carbides which can be distinguished from the white and dark region present in the image. The dark phase can be identified as Cr-rich $M_{23}C_6$, while the Nb-rich NbC phases appear as white regions due to the fact that Nb has greater atomic weight than Cr (Almeida, et. al., 2003).



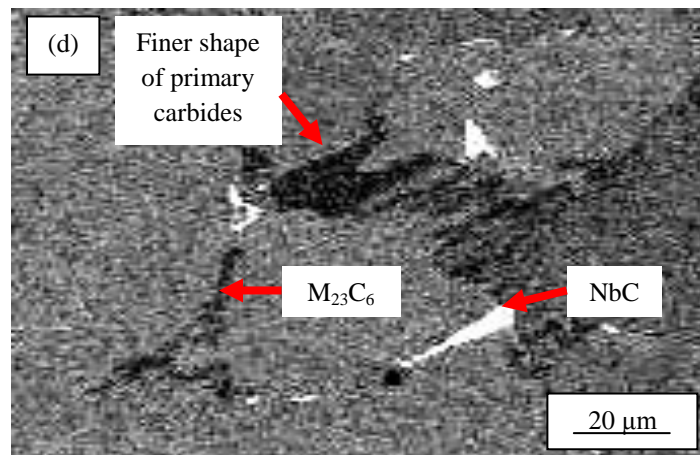
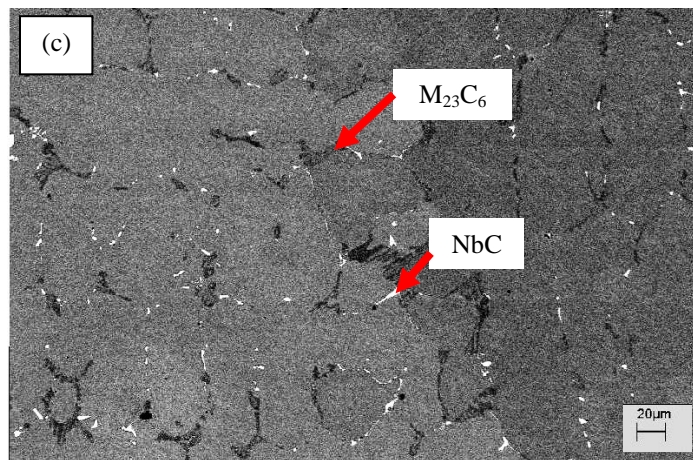
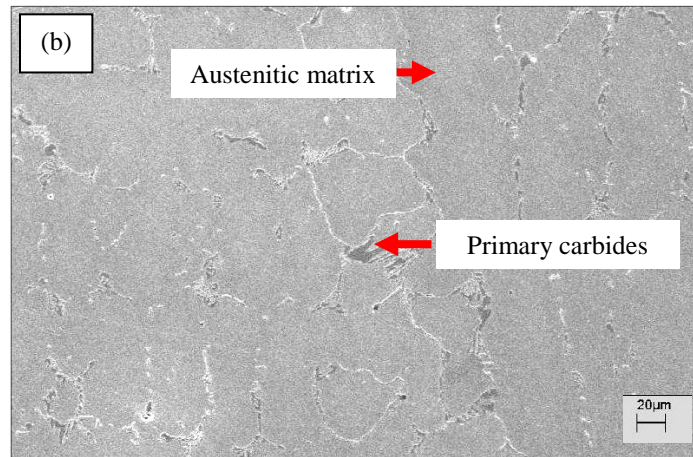


Figure 4.1: Microstructure of as-cast material; (a) optical microscope (OM) image of sample etched in glycergia; (b) secondary electron (SE) image; (c) backscatter electron (BSE) image; (d) the fine and feathery shape of the microstructure in the as-cast sample.

Energy Dispersive Spectroscopy (EDS) is done to confirm and determine which region between the dark and white that has the highest niobium or chromium concentration. It is done by SEM with spot mode at the specific white or dark region. X-ray analysis of both types of carbides (Figure 4.2), indicates that the white regions are rich in Nb, whereas the dark regions are rich in Cr.

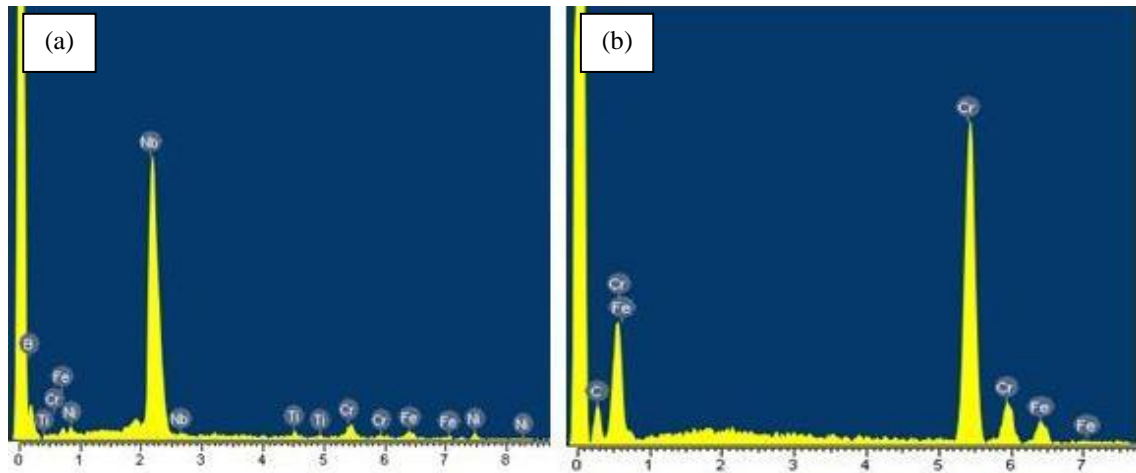
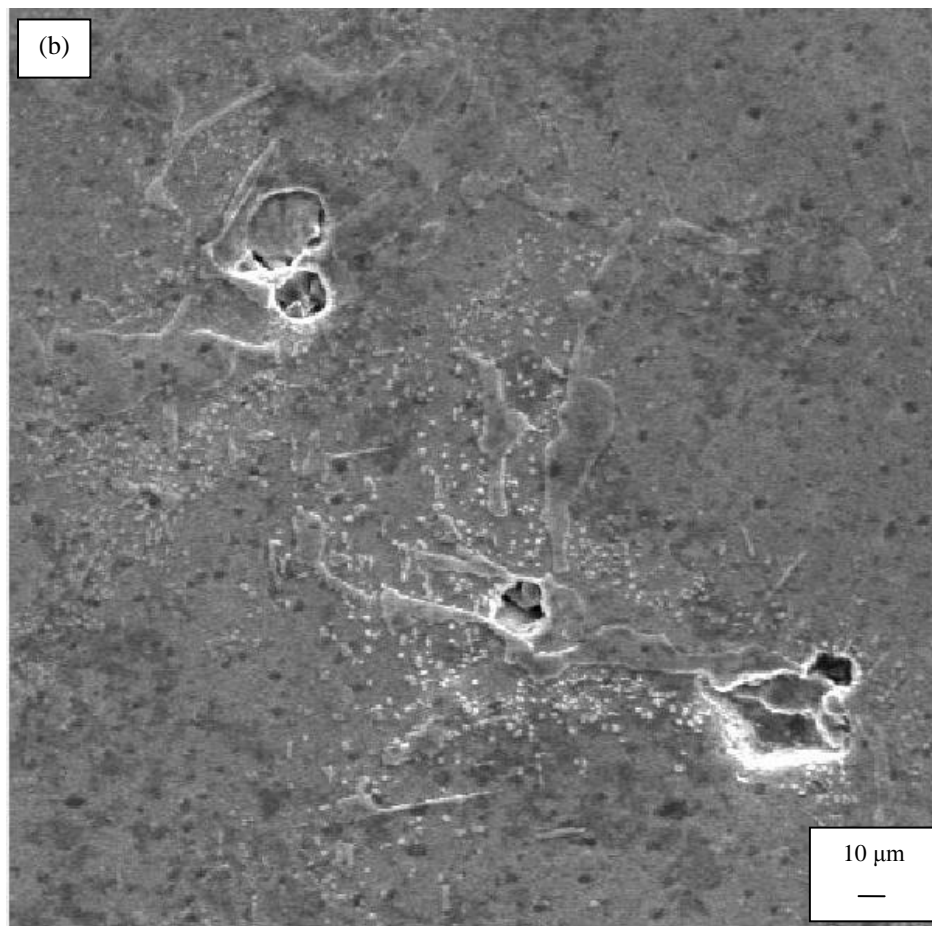
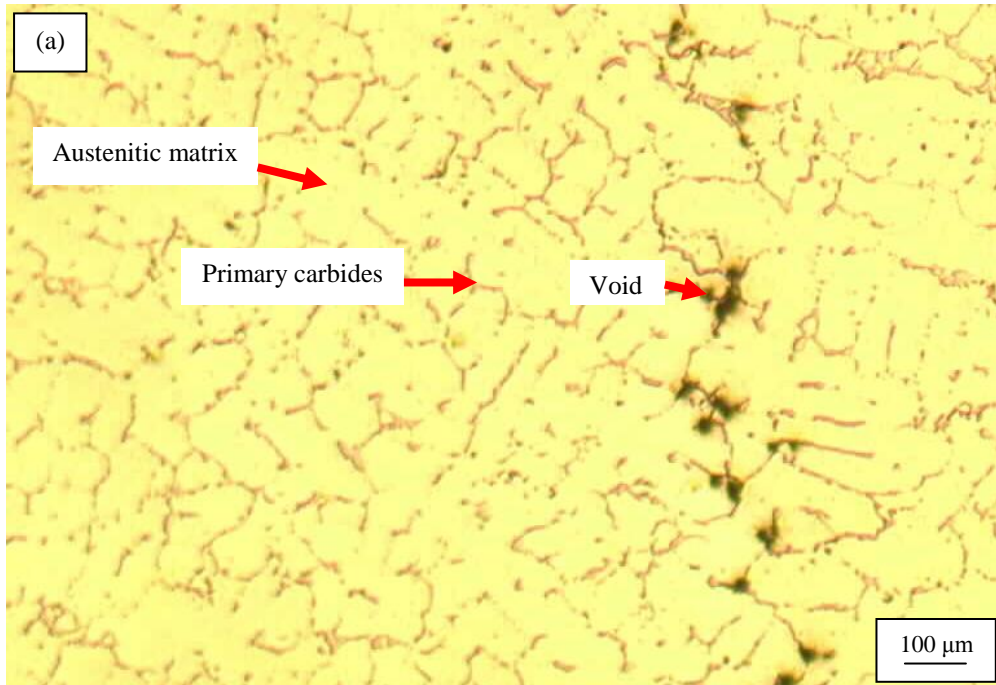


Figure 4.2: Spectra obtained by SEM with spot mode; (a) punctured at white regions; (b) punctured at dark regions.

Figure 4.3a shows the general appearance of the microstructure of the creep tested sample under the optical microscope (OM) image, while Figure 4.3b shows the secondary electron microscope (SEM) image of the creep tested sample magnified to a specific microstructure from the creep tested sample (Figure 4.3a) and Figure 4.3c is a backscatter electron (BSE) image of the magnified microstructure with the various types of precipitates labeled. Identification of coarse precipitates was done by the backscatter electron (BSE) imaging and energy dispersive spectroscopy (EDS). There were two types of precipitates present in the material (Abdul Wahab, Kral, 2005).

- $M_{23}C_6$ – It is rich in Cr and it also has a combination of various types of metal and was presented as M_{23} .
- NbC – It is called NbC and is rich with Nb.



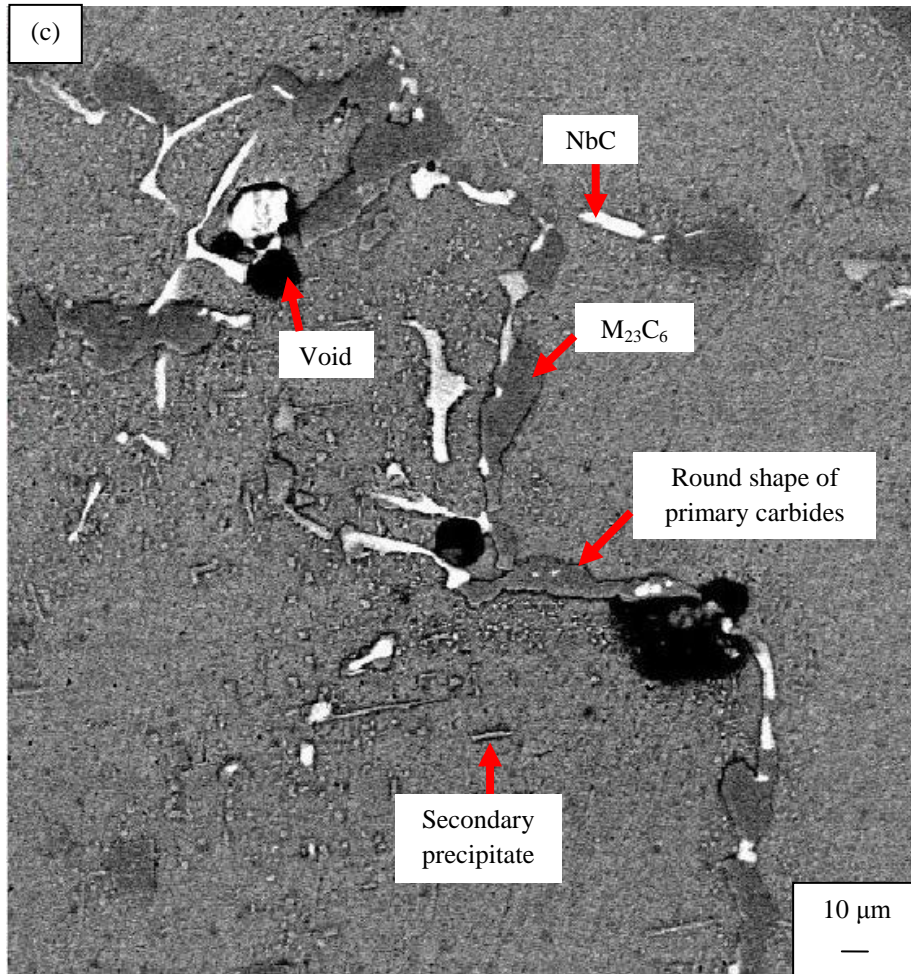


Figure 4.3: Microstructure of creep-tested material; (a) optical microscope (OM) image of sample etched in glycergia; (b) secondary electron (SE) image; (c) backscatter electron (BSE) image identifying two precipitate types $M_{23}C_6$ and NbC.

Previous work by Abdul Wahab and Kral, stated that the Cr-rich $M_{23}C_6$ appeared both intragranularly as fine precipitates and along the grain boundaries as coarse intergranular precipitates while NbC are found along the grain boundaries. TiC predominantly occurred intragranularly.

Distinctive comparison between the images from the as-cast (Figure 4.1) and the creep-tested samples (Figure 4.3) could be seen from the shape of the primary carbides present in both samples and the presence of additional microstructure in the form of

small needle like secondary carbides structures in the creep-tested samples (Figure 4.3). The shape of the primary carbides ($M_{23}C_6$ and NbC) in the creep-tested sample is much rounder (Figure 4.3c) than compared to the fine shape (Figure 4.1d) of the primary carbides in the as-cast sample.

Additional microstructure formed in the form of a series of small needle like secondary carbides structures were also detected in the creep-tested BSE images (Figure 4.3c) when compared to the as-cast BSE images (Figure 4.1c-d).

There was no void visible in the as-cast sample (Figure 4.4a) and voids were detected in the creep-tested sample (Figure 4.4b).

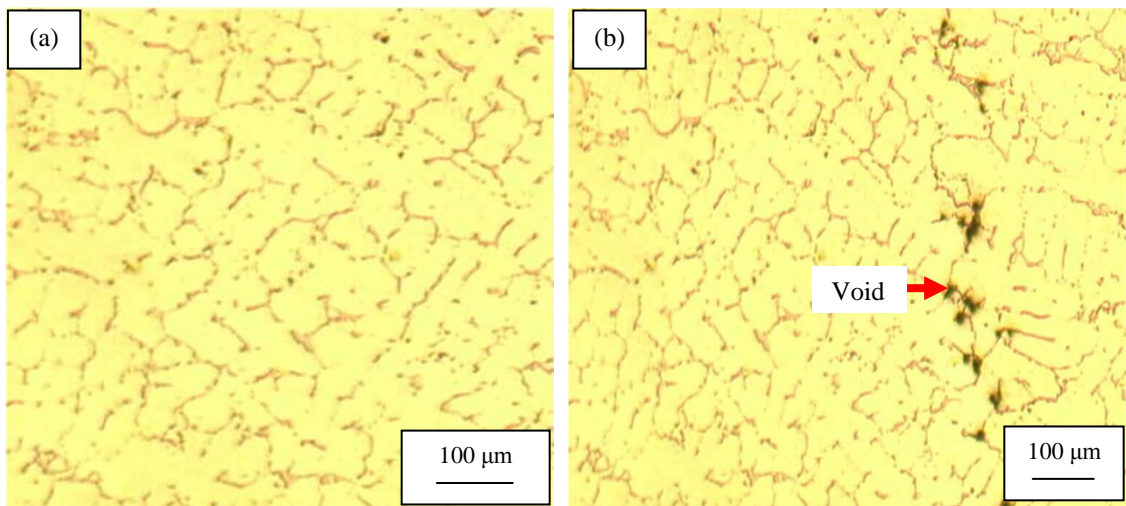


Figure 4.4: Optical microscope image; (a) as-cast sample; (b) creep-tested sample.

To further study the pattern of the voids formed in the creep-tested samples, optical images were taken from the four creep-tested samples. Figure 4.5 shows the optical microscope images of voids in sample 320, 321, 322 and 326 of the creep-tested samples. The voids seemed to occur in groups or clustered together.

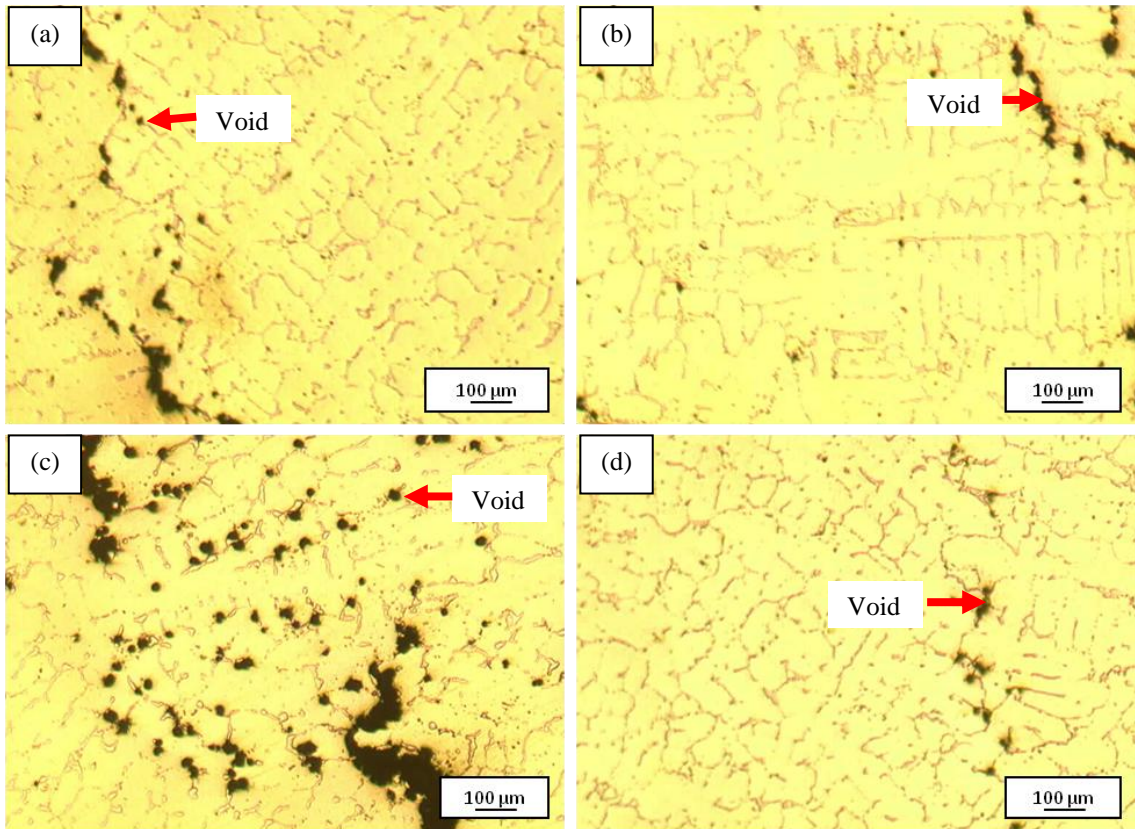


Figure 4.5: Optical microscope image of microstructure in creep-tested samples showing voids; (a) sample 320; (b) sample 321; (c) sample 322; (d) sample 326.

Backscattered electron (BSE) image from the creep-tested sample was also taken to further characterize the formation of voids as shown in Figure 4.6. From the figure, the voids seemed to occur totally on the $M_{23}C_6$ and no creep voids were detected made sole contact with NbC.

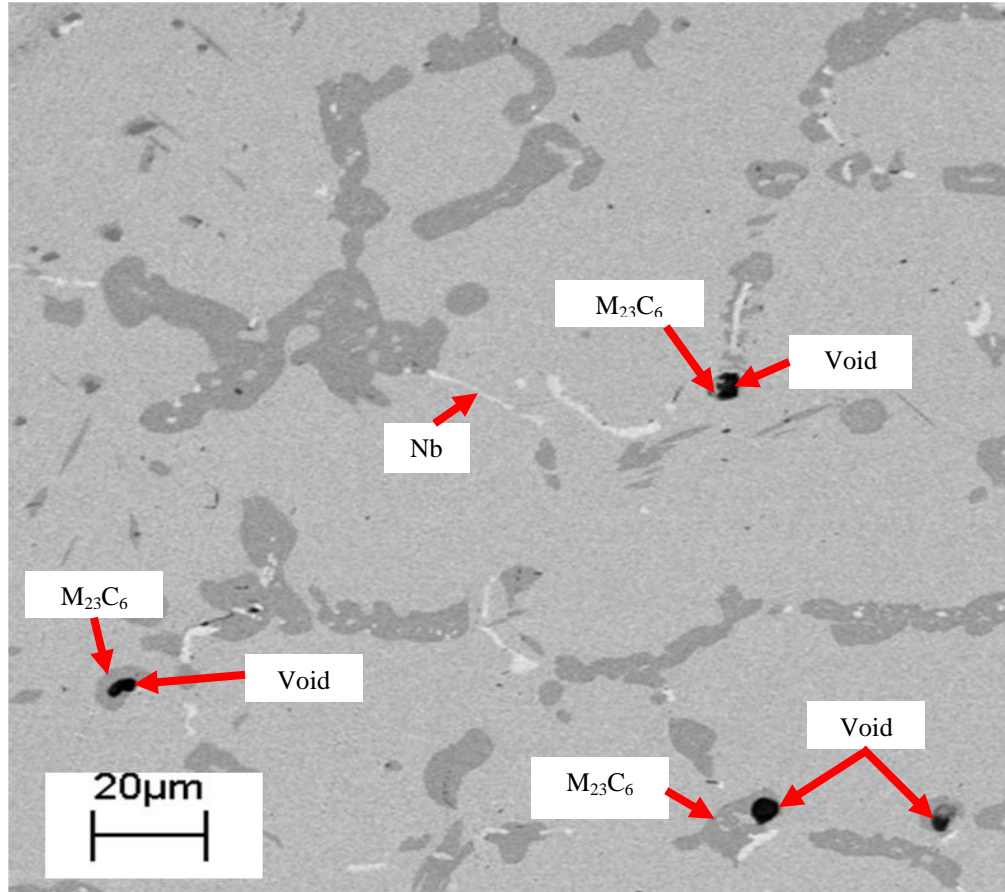


Figure 4.6: Backscattered image showing the void locations.

Table 4.1 shows the average particle size and the percentage area measured by using NIH ImageJ and then compared with Interception method as in the ASTM standards. Creep-tested sample 321 had been chosen randomly to be measured. It was to make sure that the average particle size and the percentage area obtained from NIH ImageJ were accurate as obtained by the ASTM Intercept method. From Table 4.1, the largest percentage difference between the two methods was only about 2 percents. Therefore it is proved that NIH ImageJ is as reliable as the ASTM Intercept method (see Appendix B) in obtaining the average particle size and the percentage area as it is easier and faster to obtain the values when compared to the ASTM Intercept method.

Table 4.1: Average particle size and percentage area of creep tested sample 321, measured by using the NIH ImageJ and ASTM Intercept method.

Sample	Average Particle Size (μm^2)		Percentage Area (%)	
	Chromium	Niobium	Chromium	Niobium
NIH ImageJ	25.66	7.37	6.92	2.92
Intercept Method	25.71	7.52	6.88	2.90
Difference (%)	0.19	1.99	0.58	0.68

The average particle size and percentage area of the primary carbides present in the as-cast and creep-tested samples of 320, 321, 322 and 326 (see Appendix B) were measured by NIH ImageJ were shown in Table 4.2 and Figure 4.7. From Figure 4.7, the average particle size for both the primary carbides in the creep-tested samples, decreased from the original average particle size of the primary carbides in the as-cast sample. The average particle size of Cr and Nb in the as-cast sample decreased from 41.58 and 46.64 μm^2 to 31.39 and 9.19 μm^2 in sample 320, 25.66 and 7.37 μm^2 in sample 321, 28.65 and 4.95 μm^2 in sample 322 and, 27.19 and 9.11 μm^2 in sample 326 respectively. Meanwhile, the percentage area of Cr and Nb in the as-cast sample decreased from 6.94 and 5.05 percents to 6.44 and 3.37 percents in sample 320, 6.92 and 2.92 percents in sample 321, 6.91 and 3.47 percents in sample 322 and, 5.75 and 3.44 percents in sample 326 respectively. From the result obtained, the most obvious decrease in the average particle size and percentage area was in the NbC.

Table 4.2: Average particle size and percentage area of the as-cast sample and creep-tested samples of 320, 321, 322 and 326.

Sample	Average Particle Size (μm^2)		Percentage Area (%)	
	Chromium	Niobium	Chromium	Niobium
As-cast	41.58	46.64	6.94	5.05
320	31.39	9.19	6.44	3.37
321	25.66	7.37	6.92	2.92
322	28.65	4.95	6.91	3.47
326	27.19	9.11	5.75	3.44

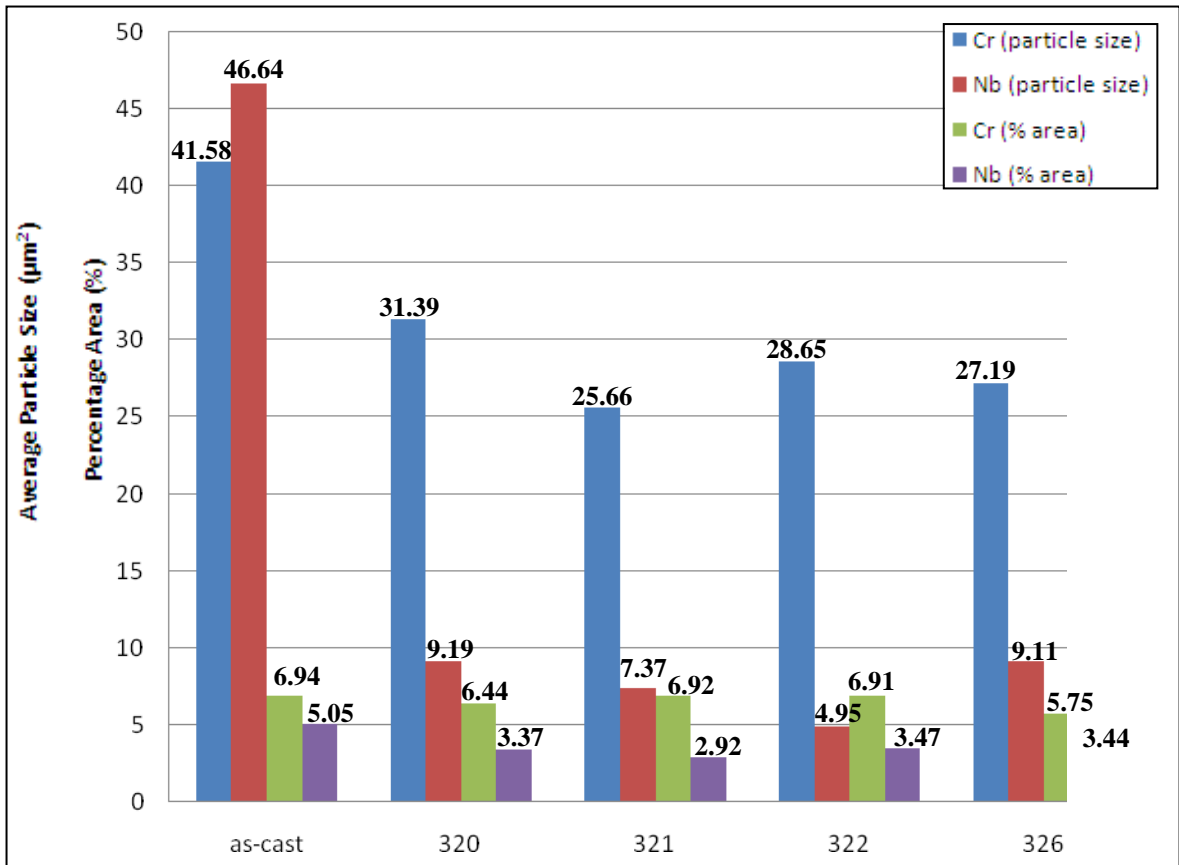


Fig. 4.7: Average particle size and percentage area of Cr and Nb in the as-cast and creep-tested samples.

CHAPTER 5

CONCLUSION AND RECOMMENDATION

The effect of creep could be seen by comparing the transformation of the microstructure in the creep-tested samples with the as-cast sample. It was found that the microstructure in the as-cast samples consisted of an austenitic matrix and a network of two types of primary carbides (chromium and niobium), whereas that of the creep tested materials in addition by having the primary carbides also exhibit a fine dispersion of small needle like structure; decomposition of primary carbides into secondary carbides was found to occur as creep progressed. Exposure at the service temperature may promote the dissolution of primary carbides and development of a fine array of secondary carbides precipitated from the highly supersaturated matrix (Rodriguez, et. al., 2000).

The shape of the primary carbides ($M_{23}C_6$ and NbC) in the as-cast sample is finer and more faceted than the rounder shape of the primary carbides in the creep-tested samples. It is because of with increasing service time and temperature; the primary carbides tend to coarsen into rounder precipitates (Abdul Wahab, Kral, 2005).

The decrease of chromium's average particle size and percentage area is believed to be due to Cr being dissolved into the matrix forming the precipitation of the secondary $M_{23}C_6$ type carbide (Rodriguez, et. al., 2000). On the other hand, the high amount of decrease in the average particle size and percentage area of niobium is believed to be due to Nb is dissolved in the steel (Moon, et. al. 2007). When Nb is dissolved in matrix, new bonds are made such as titanium carbide, TiC. This was proved from previous work done by Moon, Kim, Jeong and Lee, when there is presence of Nb, the solute concentration of Ti in the matrix was increased. In this project, 62.84 weight

percent of Nb in the as-cast sample decreased to 43.78 weight percent in the creep-tested sample, while 0.6 weight percent of Ti in as-cast sample increased to 4.13 weight percent in the creep-tested sample (see Appendix C).

Also by examining periodic table, it is believed that chromium which is more reactive than niobium will attract the carbons from the NbC and thus reducing the Nb average particle size. This is based on the definition of ionization energy which measures how strongly an atom holds on to its electrons and electron affinity is a measure how strongly an atom attracts additional electrons (Brown, et. al., 2003). Chromium which is located to the right of Nb in the periodic table, has an atomic radius which is smaller than Nb and also has higher electron affinity. Therefore, Cr which is more reactive than Nb, is believed to attract the carbons from NbC, thus decreasing the average particle size and percentage area of Nb. Chromium which also has higher ionization energy than Nb would be least likely to lose its electrons to Nb (see Appendix C).

There are no creep voids detected in the as-cast sample but voids seemed to form in the creep-tested samples. As time and service temperature lengthens, stress pulled apart the microstructure to form creep voids. The creep voids seemed to occur in groups or clustered together forming a line at boundaries between two grains. A possible explanation would be that creep voids are most likely to nucleate at the grain boundaries because of vacancies due to lattice mismatch between carbide and austenite (Abdul Wahab, Kral, 2005).

The main lessons gained and learned through this project was how to do metallographic sample preparation techniques, and to use various microstructure characterization techniques and tools to study material behavior. This project also gave an insight about the creep phenomena and effect of creep to the transformation of the microstructure as creep progressed through the whole life period of the reformer tubes.

This project is beneficial as it gave an understanding of how creep progressed and its effect on the reformer tube material. This would also present an opportunity for the manufacturers to further improve the metallurgy of the material so that the life of the

reformer tube could be extended. It would also provide vital information on evaluating the performance of Cr and Nb additions in creep strengthening mechanism. This project also gave a review of how microstructure characterization could be done.

For future work recommendation, the creep-tested samples could be replaced with an ex-service reformer tube material so that the transformation of the microstructure could be studied in terms of true operating conditions, as the creep-tested samples were only small representative of what the actual creep progression really occurred.

REFERENCES

- Azmi Abdul Wahab, Milo V. Kral, 2005, "3D Analysis of Creep Voids in Hydrogen Reformer Tubes," *Materials Science and Engineering A* **412**: 222-229
- Barbela, G D, 1991, "Phase Characterization in Two Centrifugally Cast HK Stainless Tube," *Materials Characterization* **26**: 1-7
- Barbela, G D, 1991, "Role of Nb in Modifying the Microstructure of Heat Resistant Cast HP Steel," *Materials Characterization* **26**: 193-197
- Barbela, G D, 1991, "Niobium Additions in HP Heat Resistant Cast Stainless Steels," *Materials Characterization* **29**: 387-396
- Bogdan Piekarski., 2001, "Effect of Nb and Ti Additions on Microstructure, and Identification of Precipitates in Stabilized Ni-Cr Cast Austenitic Stainless Steel," *Materials Characterization* **47**: 181-186
- Borges RMT, de Almeida LH, 1999, "Microstructure of a Centrifugally Cast Modified-HP Steel Tube with Yttrium Additions," *Acta Microsc Suppl A* **8**: 251-202
- Brown, LeMay, Bursten, 2003. *Chemistry the Central Science*, New York, Prentice Hall
- Chris Maharaj, Clement A.C. Imbert, John Dear, 2008, "Failure Analysis and Creep Remaining Life of Hydrogen Reformer Outlet Pigtail Tubes," *Engineering Failure Analysis*
- D.R.H Jones, 2004, "Creep Analysis of Overheated Boiler, Superheater and Reformer Tubes," *Engineering Failure Analysis* **11**: 873-893

John Campbell, 1991, *Castings*

Joonoh Moon, Sanghoon Kim, Hongchul Jeong, Jongbong Lee, Changhee Lee, 2007, “Influence of Nb Addition on the Particle Coarsening and Microstructure Evolution in a Ti-Containing Steel Weld HAZ,” *Materials Science and Engineering A* **454-455**: 648-653

Julian Rodriguez, Sergio Haro, Abraham Velaso, Rafael Colas, 2000, “A Metallographic Study of Aging in a Cast Heat Resisting Alloy,” *Materials Characterization* **45**: 25-32

Leco Corporation, 2002, *Metallography Principles and Procedures*, St. Joseph, Miami, USA

Luiz Henrique de Almeida, Andre Freitas Ribeiro, Ian Le May, 2003, “Microstructural Characterization of Modified 25Cr-35Ni Centrifugally Cast Steel Furnace Tubes,” *Materials Characterization* **49**: 219-229.

Peter Beeley, 2001, *Foundry Technology*

Wayne Rasband. 2008 <<http://rsb.info.nih.gov/ij/index.html>>. Wikipedia Foundation Incorporated. 2008 <<http://en.wikipedia.org/wiki>>.

Robert H. Dreyfuss, 2004, *ANNUAL BOOK OF ASTM STANDARDS, SECTION THREE, Metal Test Methods and Analytical Procedures, VOLUME 03.01, Metals – Mechanical Testing; Elevated and Low Temperature Test; Metallography*, Baltimore, ASTM International

Robert H. Dreyfuss, 2004, *ANNUAL BOOK OF ASTM STANDARDS, SECTION FOURTEEN, General Methods and Instrumentation, VOLUME 14.02, General Test Methods; Forensic Sciences; Terminology; Conformity Assessment; Statistical Methods*, Baltimore, ASTM International

Soares GDA, de Almeida LH, Le May I., 1992, “Niobium Additions in HP Heat-Resistant Cast Stainless Steels,” *Materials Characterization* **29**: 387-396

William D. Callister Jr., 2003, *Materials Science and Engineering an Introduction*, New York, John Wiley & Sons

Wu XQ, Jing HM, Zheng YG, Yao ZM, Ke W, Hu ZQ., 2000, “The Eutectic Carbides and Creep Rupture Strength of 25Cr20Ni Heat-Resistant Steel Tubes Centrifugally Cast with Different Solidification Conditions,” *Materials Science Engineering A* **293**: 252-260

APPENDIX A
USING NIH IMAGEJ

NIH IMAGEJ

Measuring Cr particle size and percentage area using NIH ImageJ:

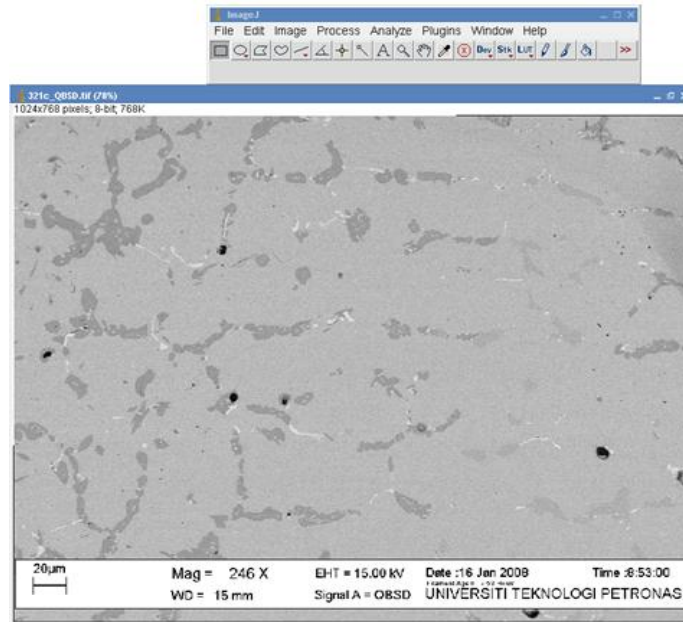


Figure A-1: BSE image of creep-tested sample loaded by NIH Image J

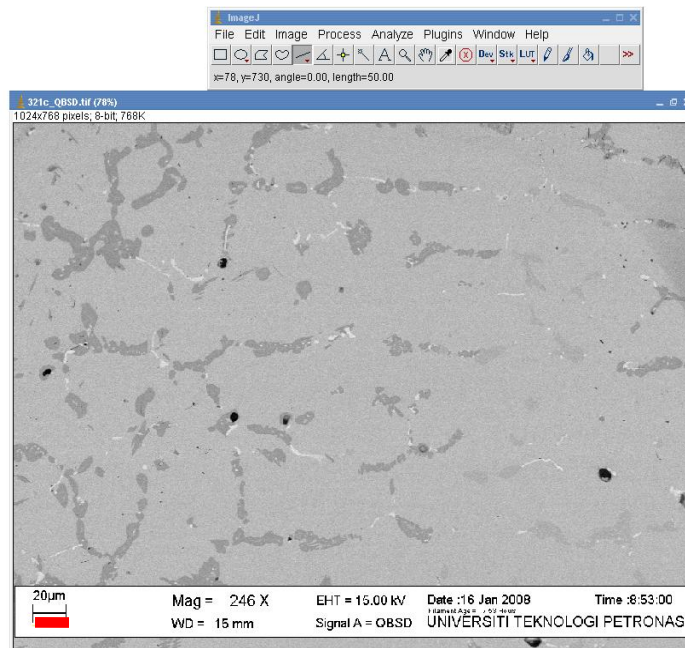


Figure A-2: Measuring length of scale (bottom left corner)

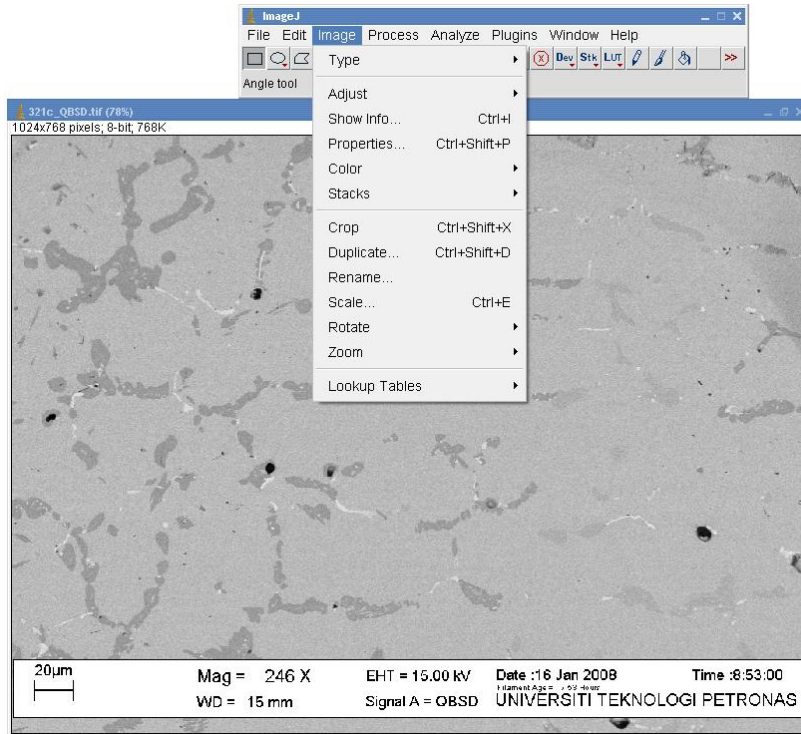


Figure A-3: Clicking at “Image” toolbar

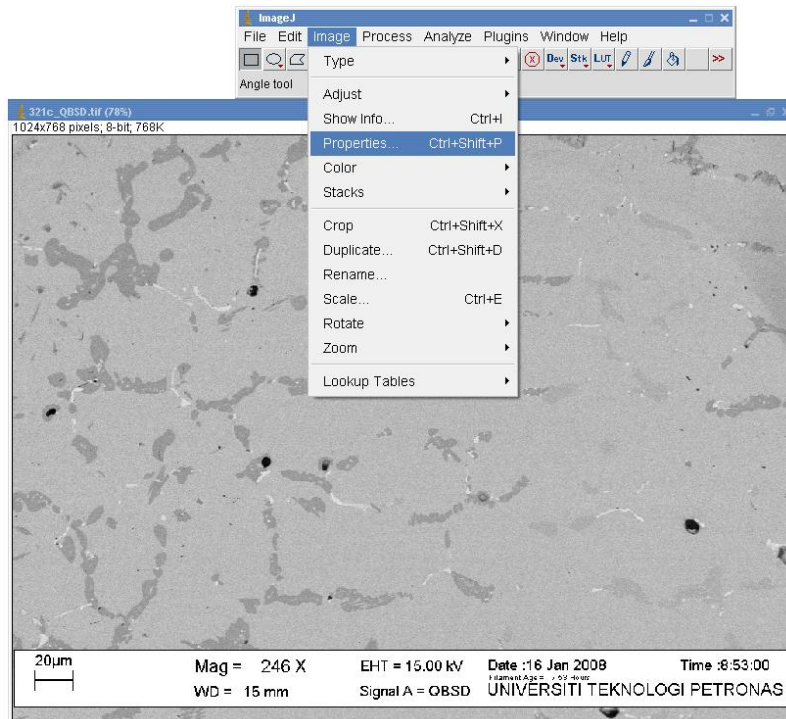


Figure A-4: Clicking at “Properties”

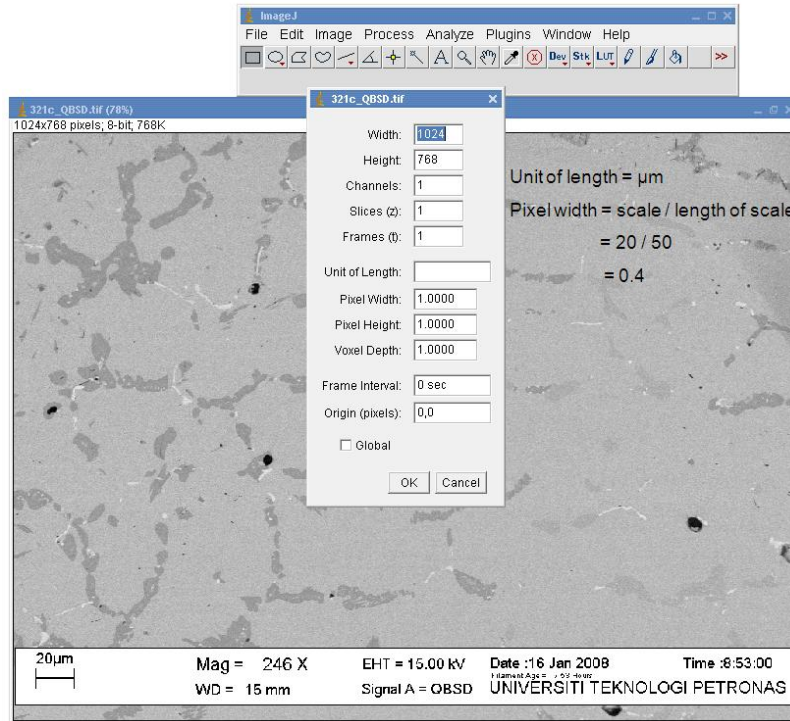


Figure A-5: Converting from pixel to unit of length

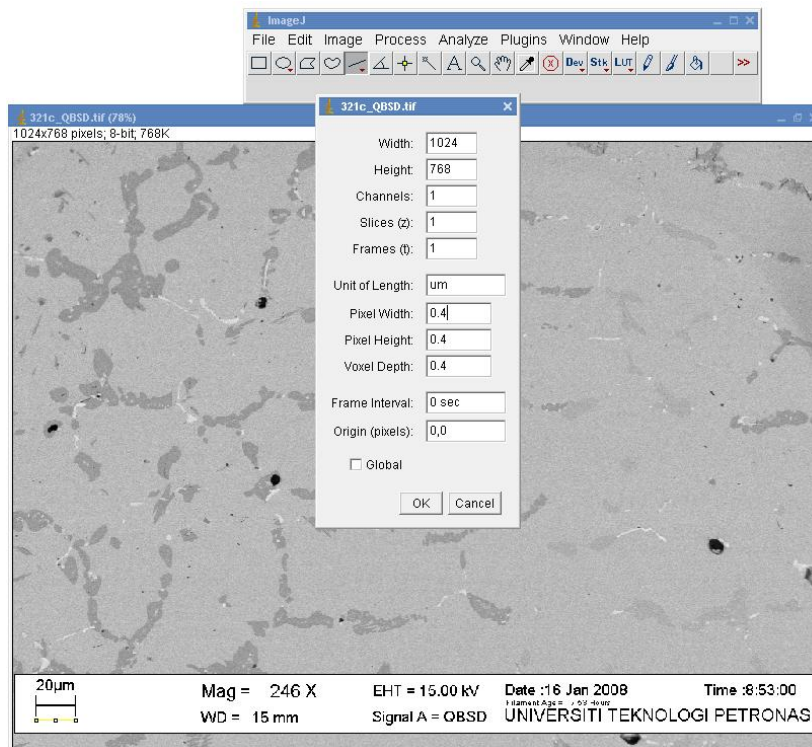


Figure A-6: Inputting the conversion factor into pop up window

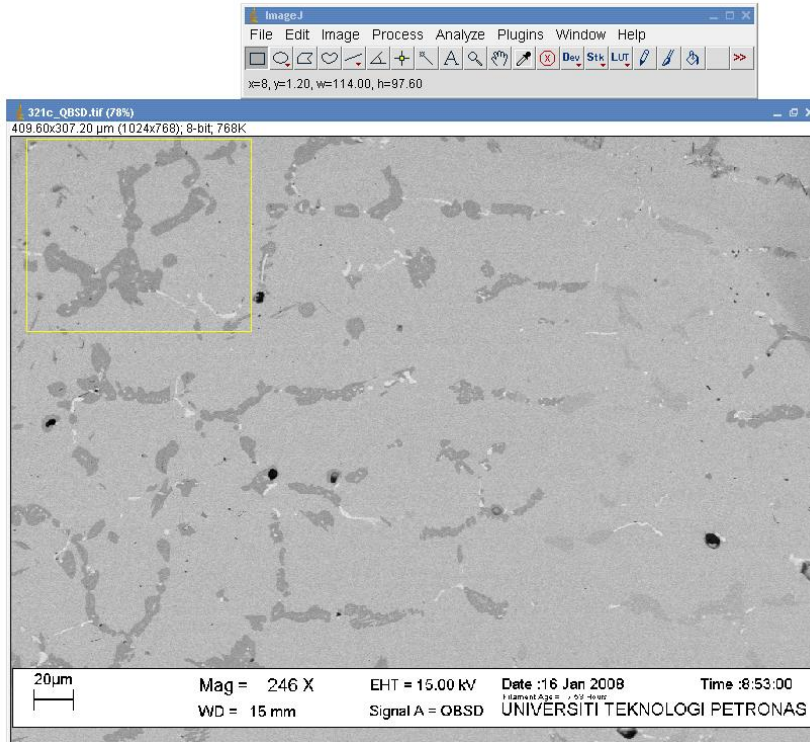


Figure A-7: Cropping a portion of the BSE image

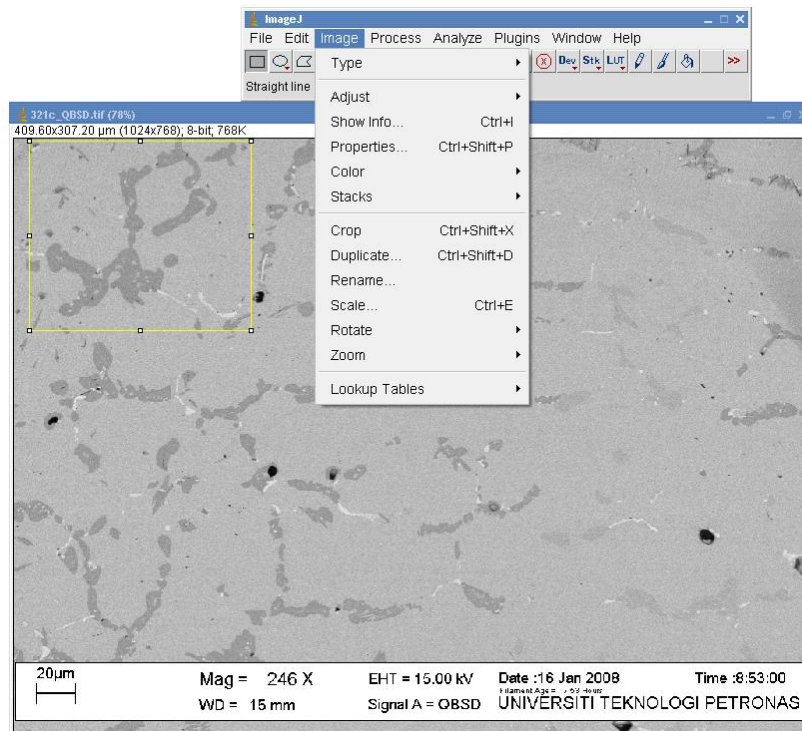


Figure A-8: Clicking at “Image” toolbar

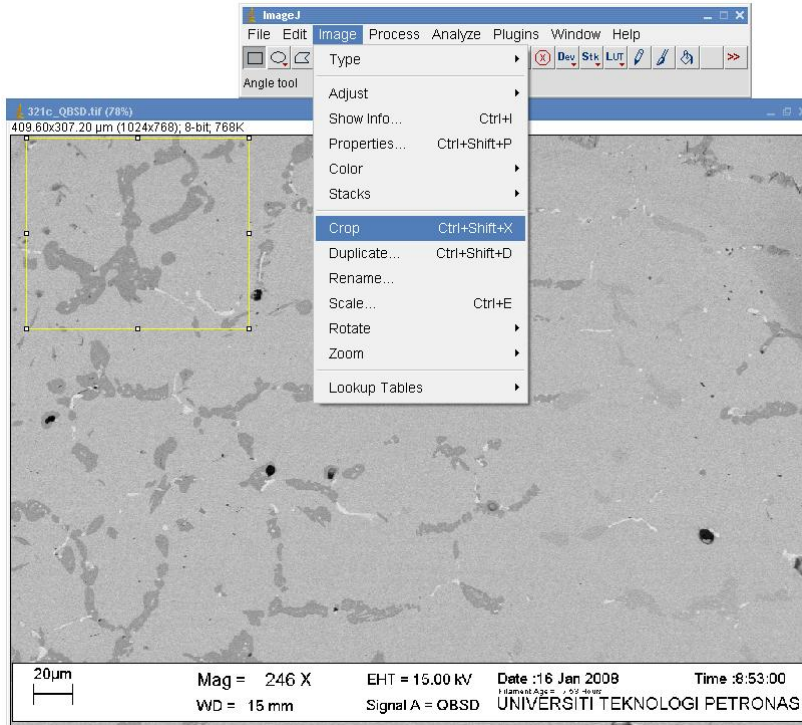


Figure A-9: Clicking at “Crop”

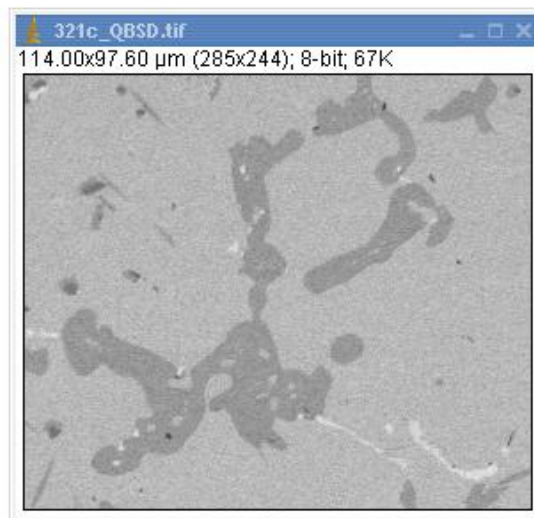
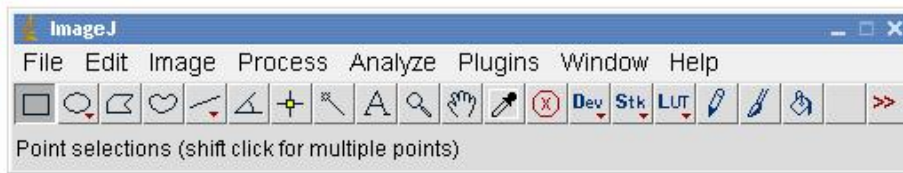


Figure A-10: Cropped BSE image to measure Cr

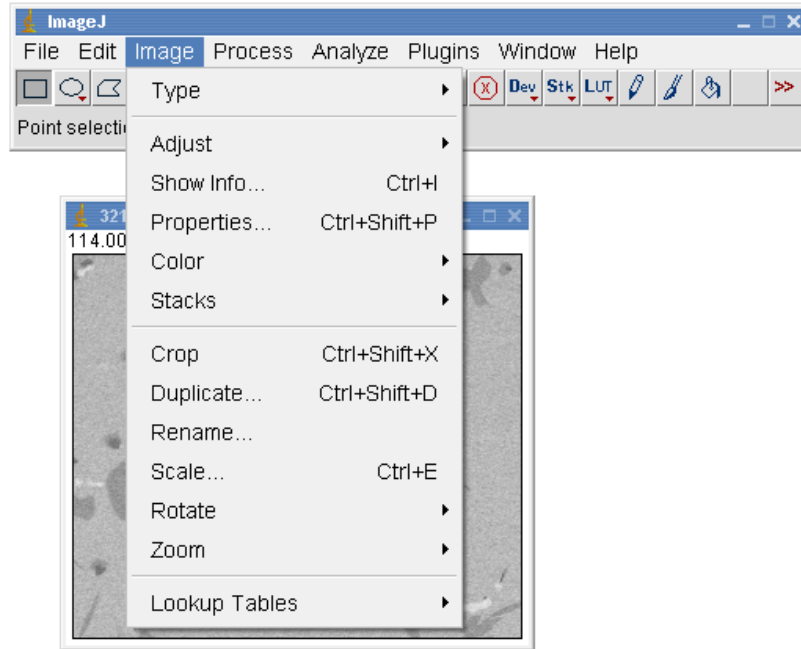


Figure A-11: Clicking at “Image” toolbar

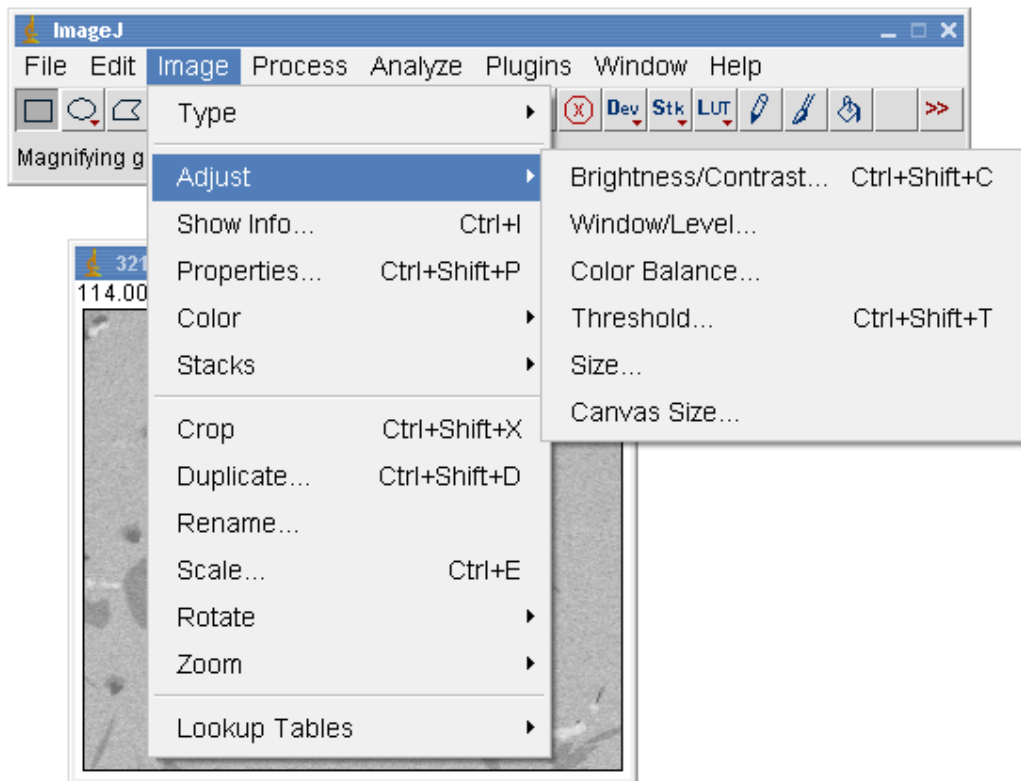


Figure A-12: Clicking at “Adjust”

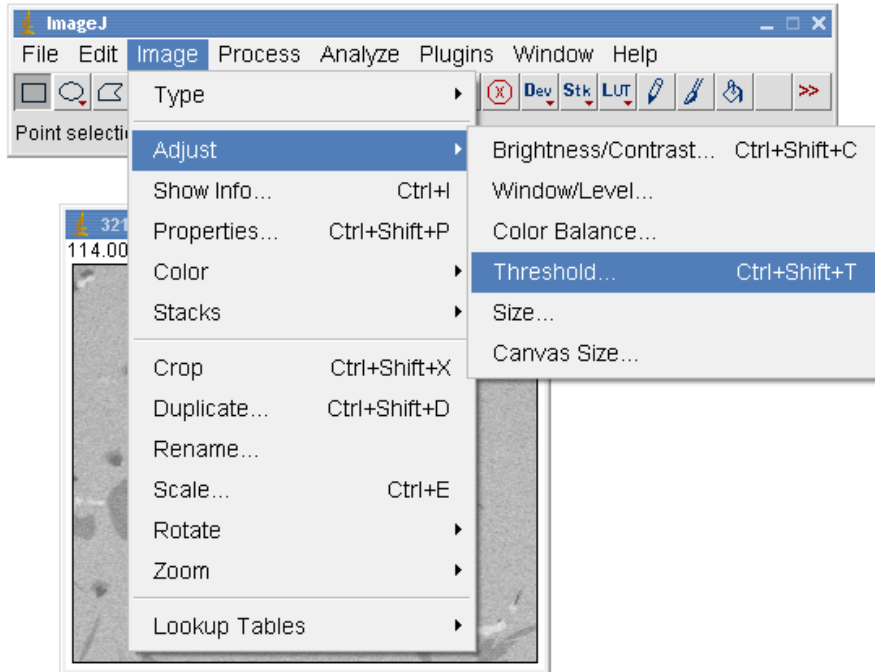


Figure A-13: Clicking at “Threshold”

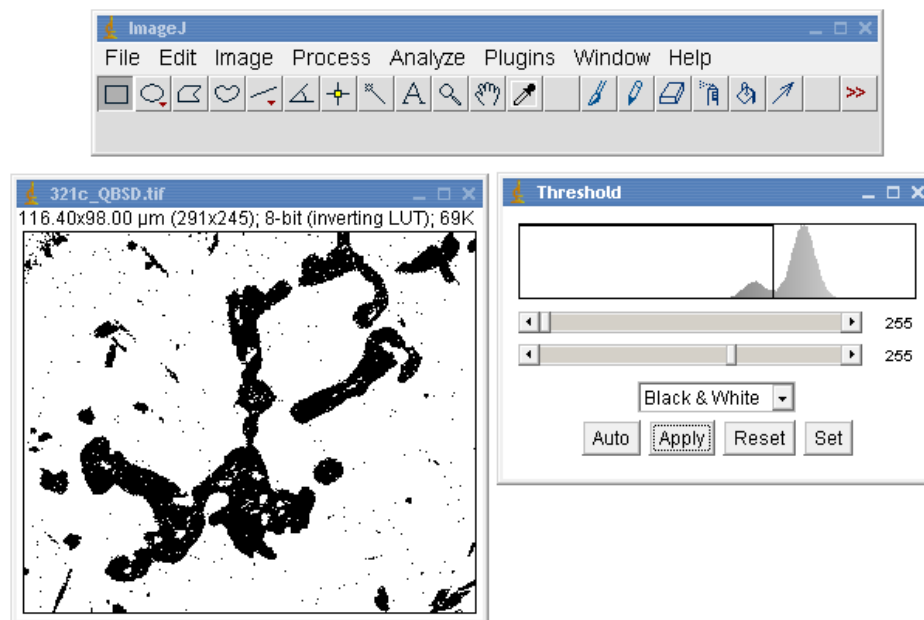


Figure A-14: Adjusting the black and white mode of “Threshold” limits to show only Cr

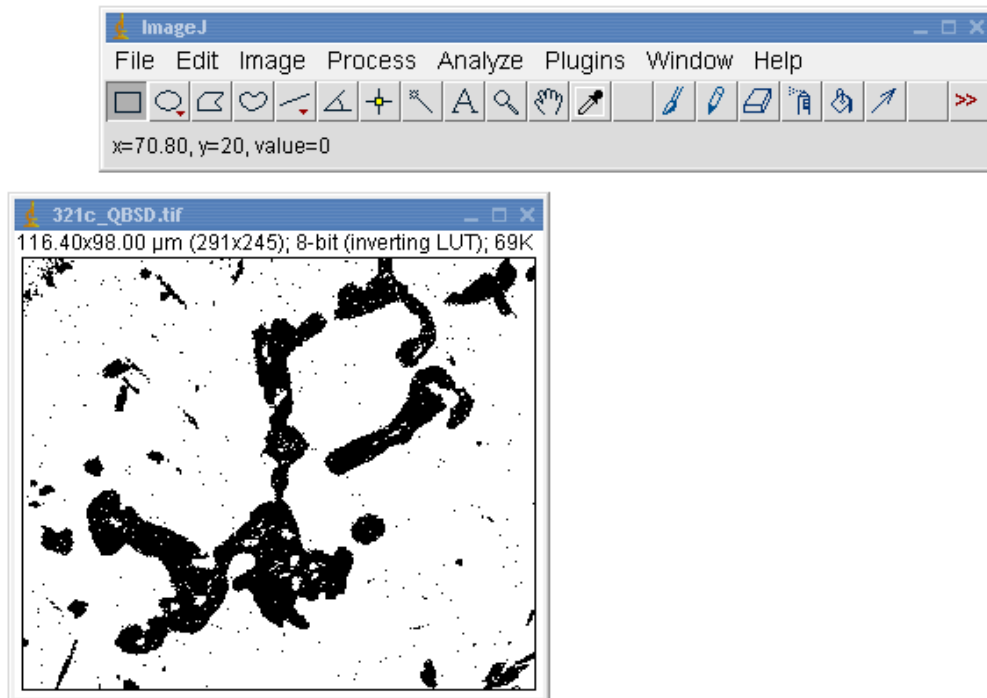


Figure A-15: Cr image (black) only appeared at pop out window

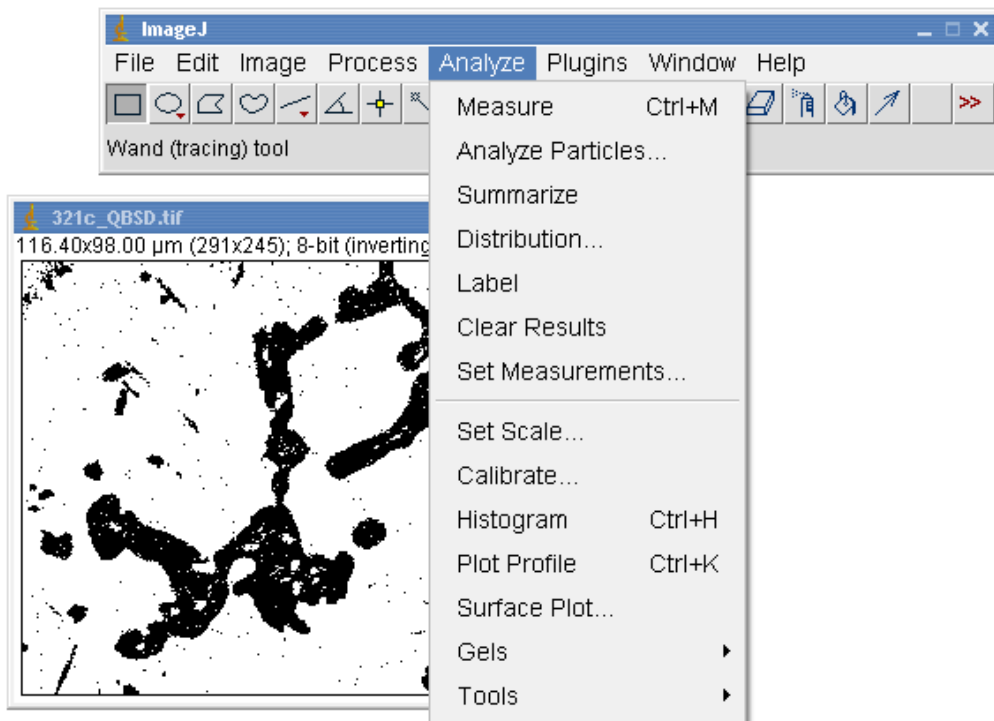


Figure A-16: Clicking at “Analyze”

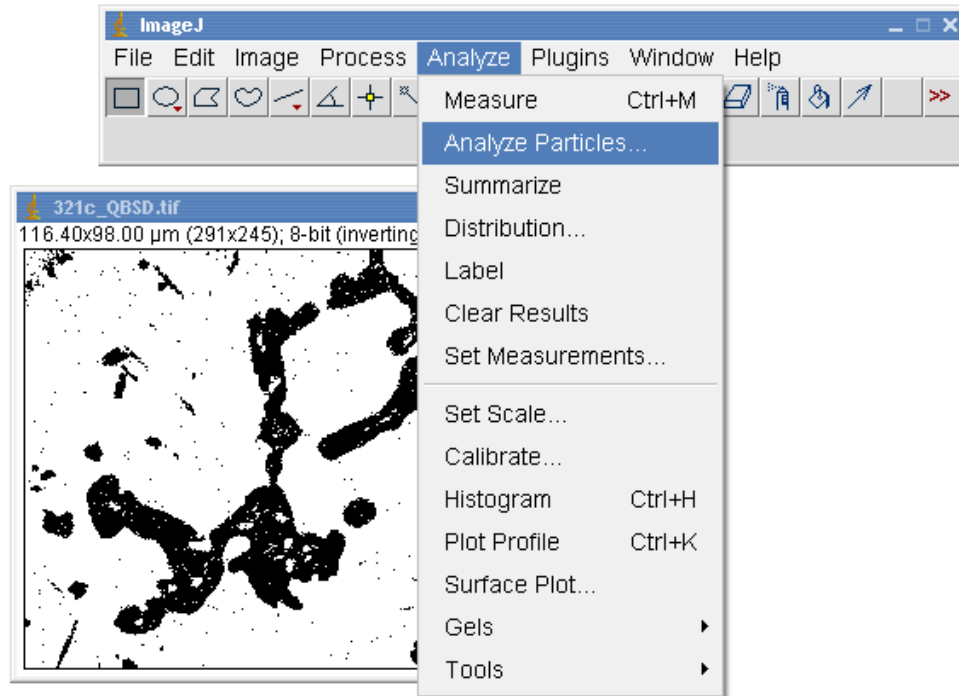


Figure A-17: Clicking at “Analyze Particle”

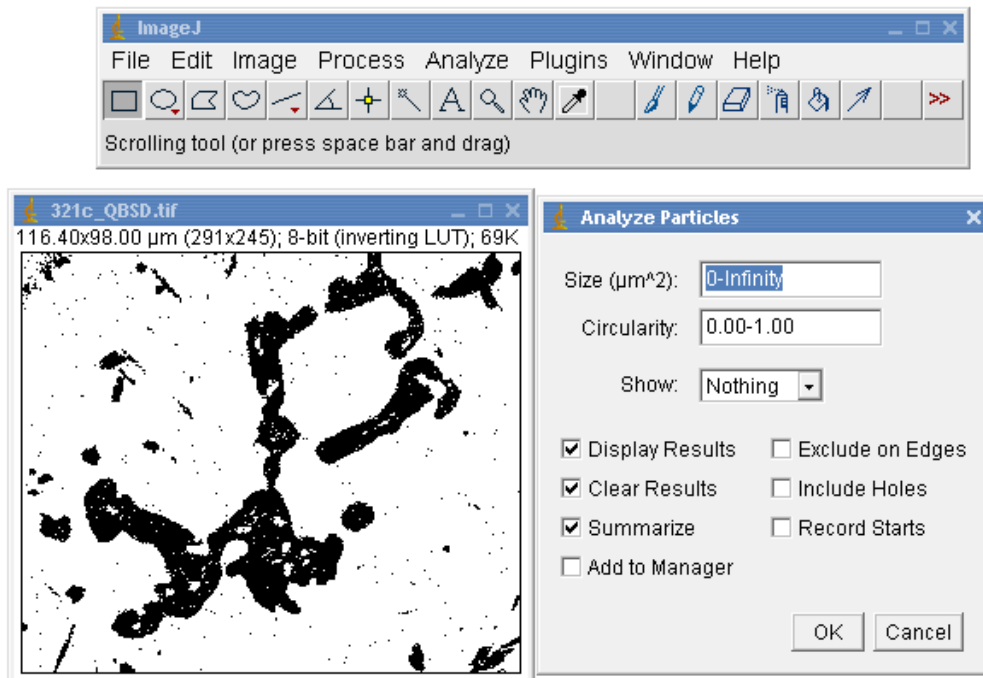


Figure A-18: “Analyze Particle” pop up window

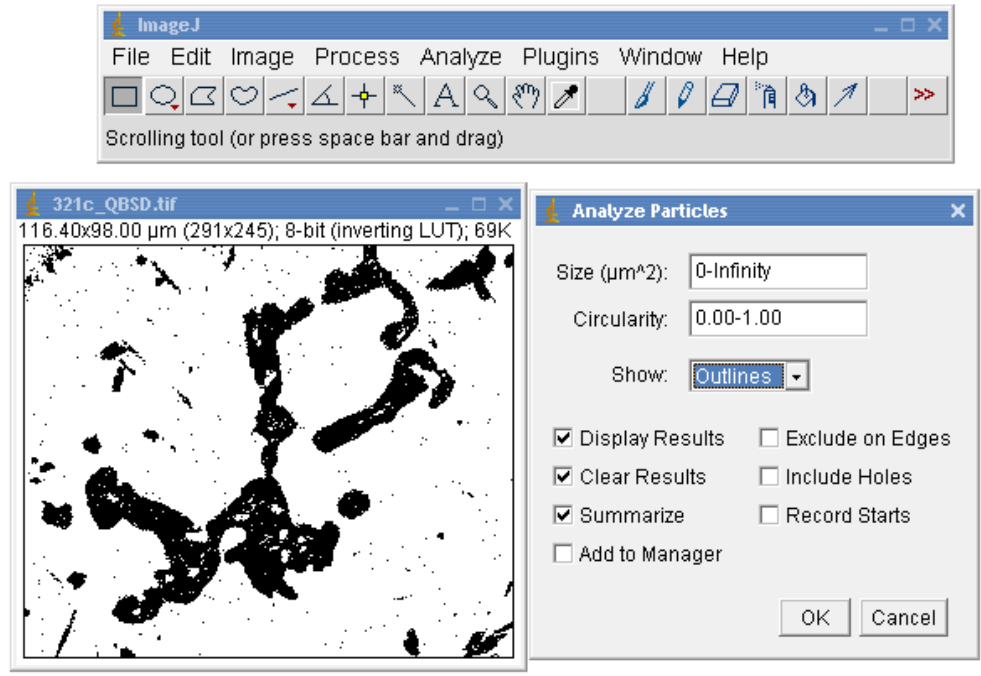


Figure A-19: Changing the “show” input box from “Nothing” to “Outlines”

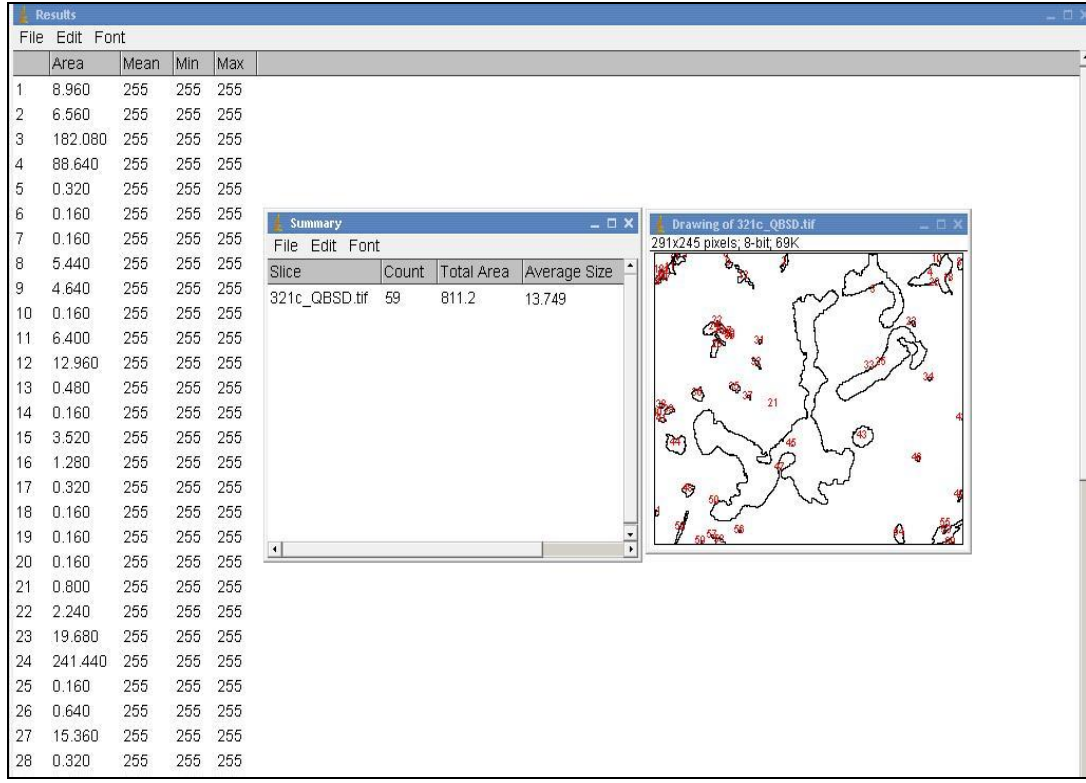


Figure A-20: Result (1-28), summary and outline numbered of the cropped Cr image

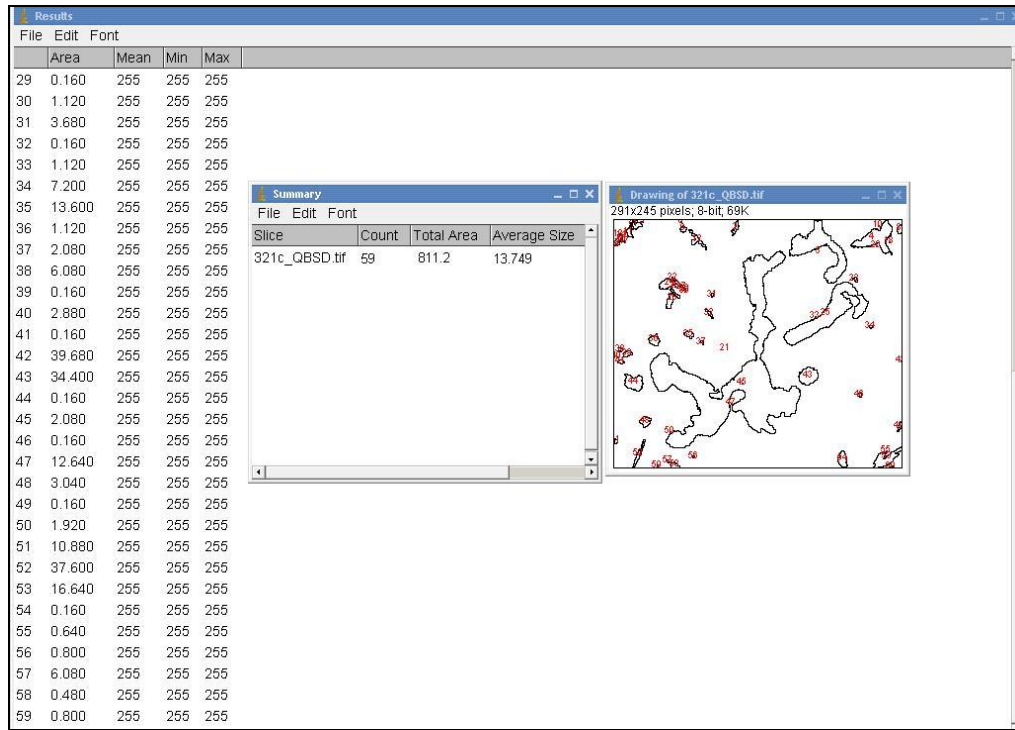


Figure A-21: Result (29-59), summary and outline numbered of the cropped Cr image

Measuring Nb average particle size and percentage area:

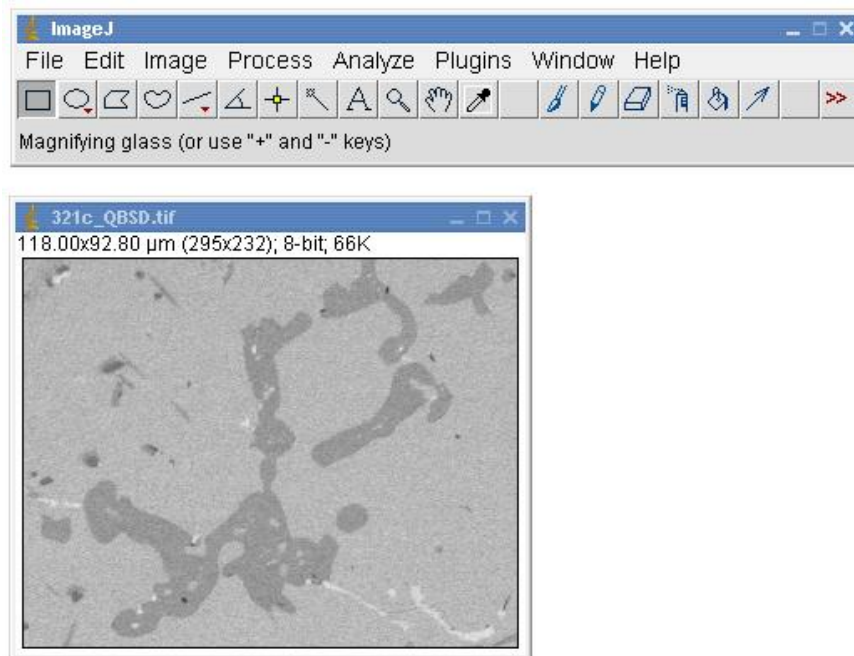


Figure A-22: Cropped BSE image to measure Nb

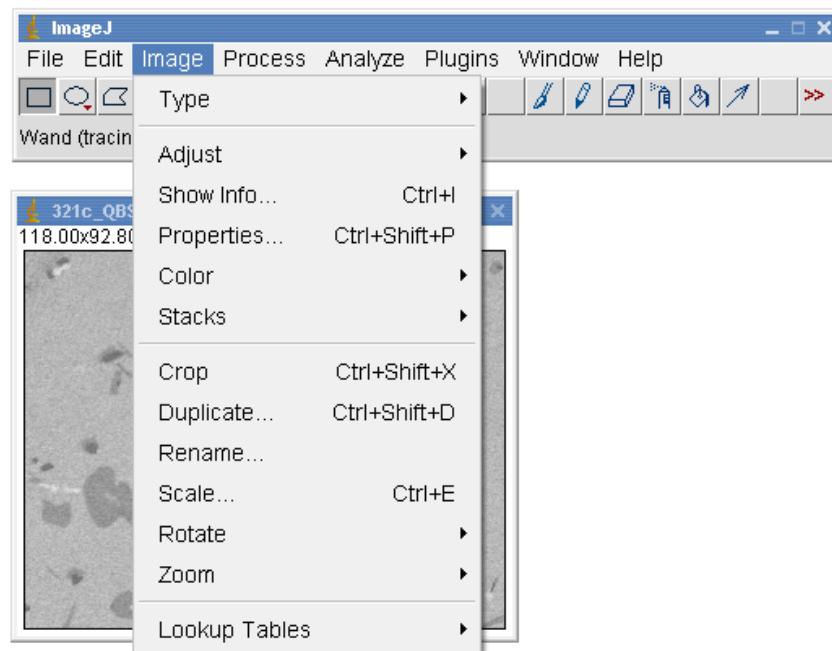


Figure A-23: Clicking at "Image" toolbar

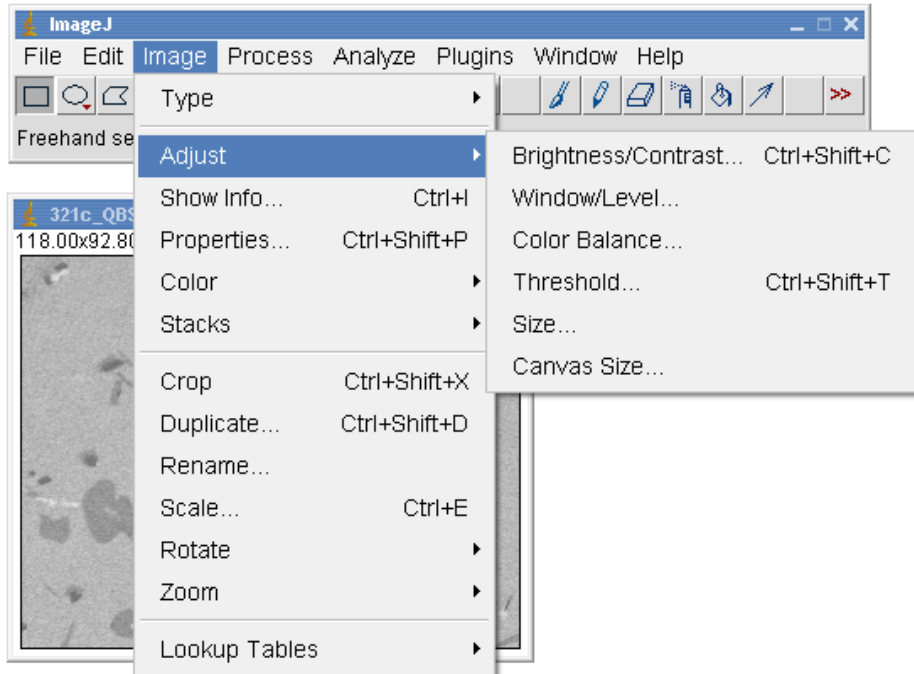


Figure A-24: Clicking at “Adjust”

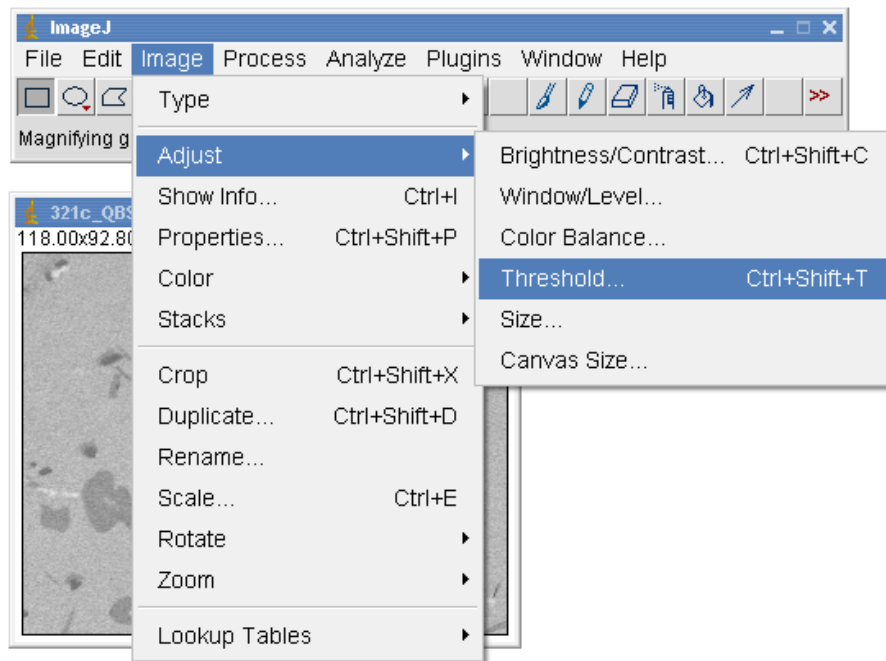


Figure A-25: Clicking at “Threshold”

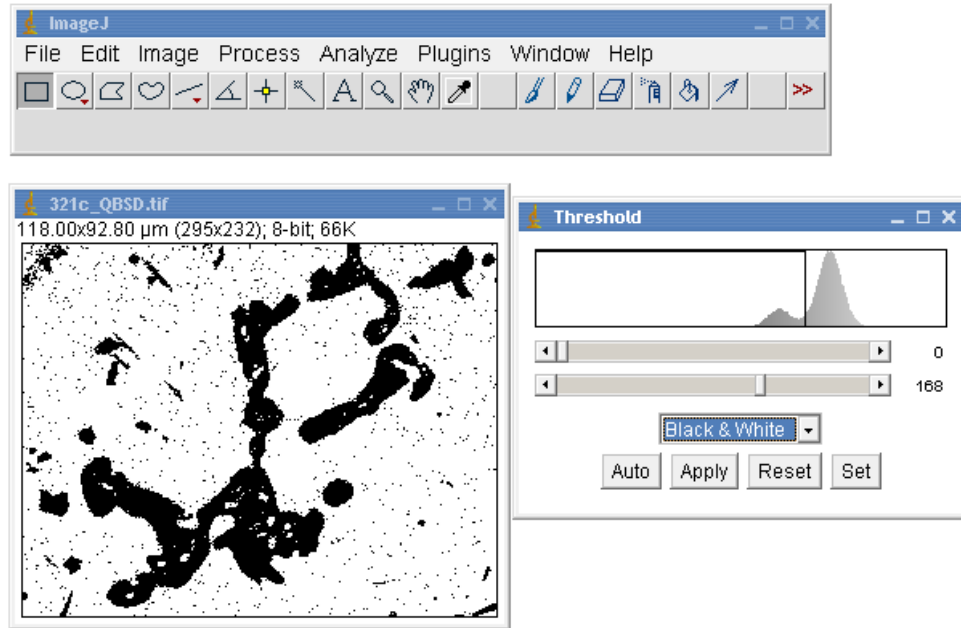


Figure A-26: Adjusting black and white mode of “Threshold” limits to show only Nb

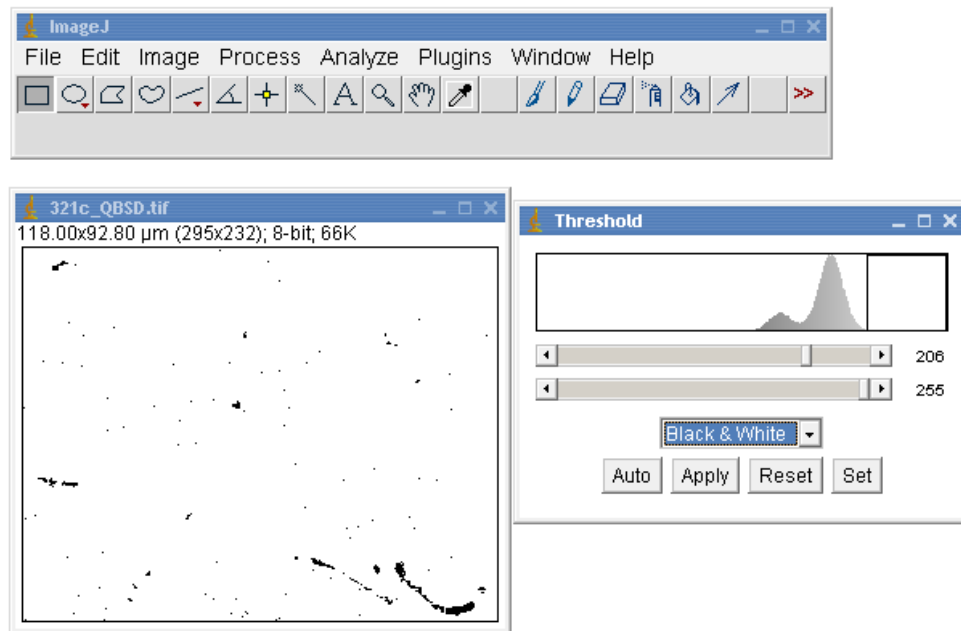


Figure A-27: Nb image (black) only appeared at pop out window

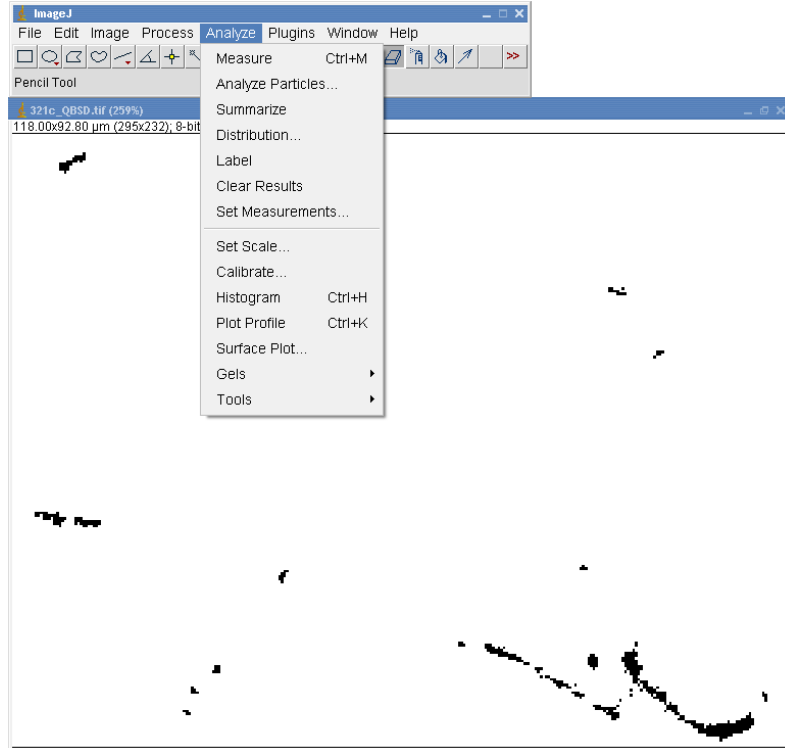


Figure A-28: Clicking at “Analyze” toolbar

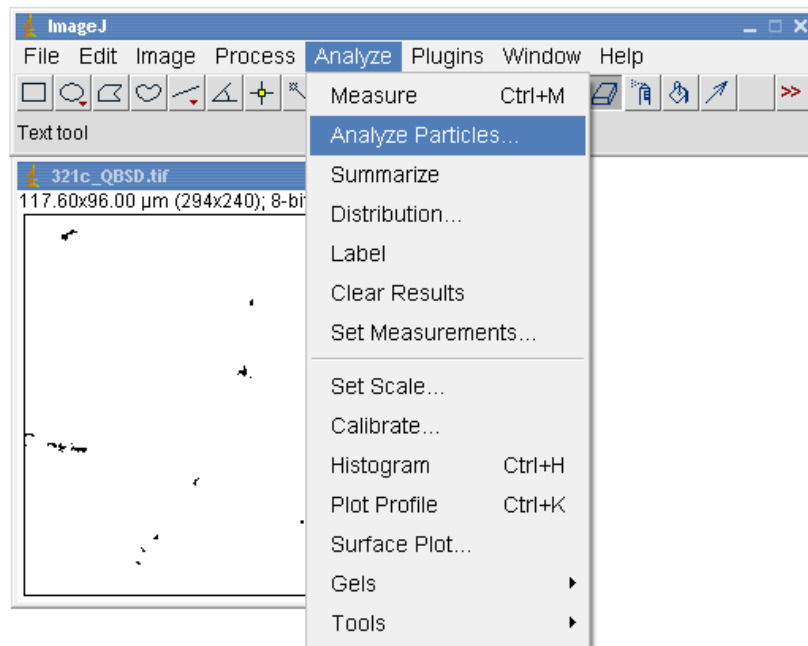


Figure A-29: Clicking at “Analyze Particles”

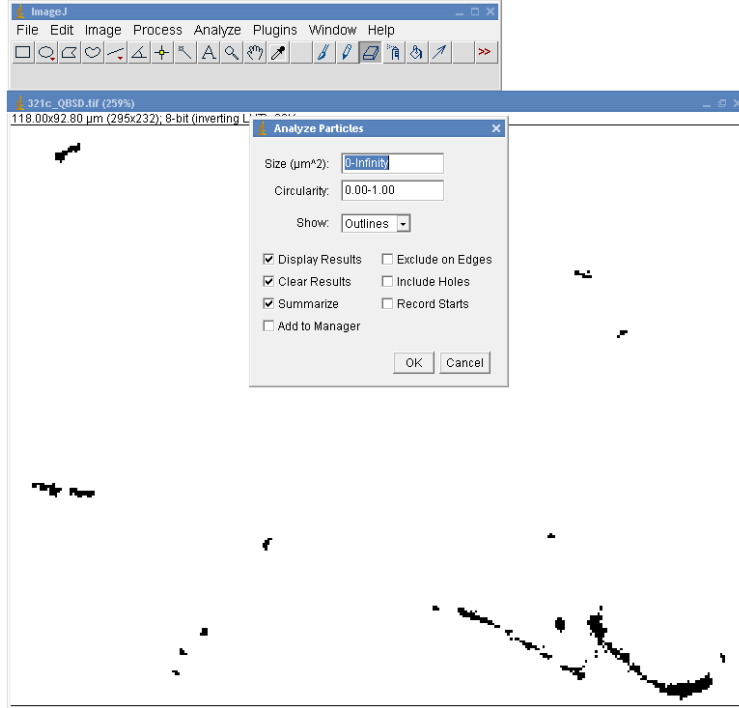


Figure A-30: Changing the “show” input box from “Nothing” to “Outlines”

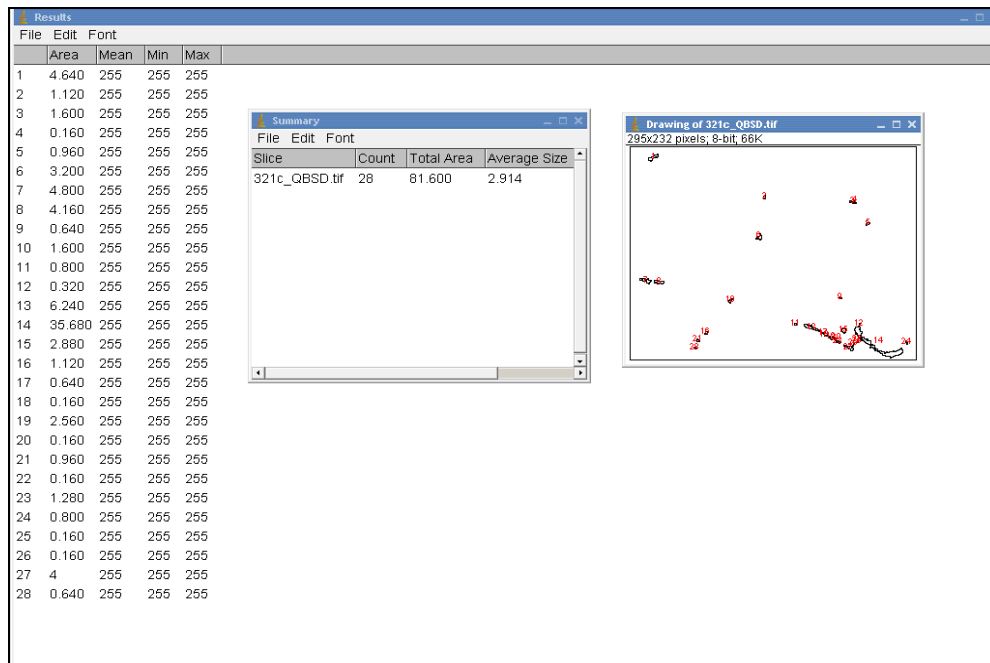


Figure A-31: Result (1-28), summary and outline numbered of the cropped Nb image

APPENDIX B

RESULTS

Table B-1: Average particle size and percentage area of creep tested sample 321, measured by using the intercept method.

Sample	Count		Particle Size (μm^2)		Total Area (μm^2)	Average Particle Size (μm^2)		Percentage Area (%)	
	Cr	Nb	Cr	Nb		Cr	Nb	Cr	Nb
A	100	270	2600.75	1439.05	161599.46	26.00	5.32	1.61	0.89
B	90	110	2540.65	1117.74	161997.53	28.93	10.16	1.56	0.69
C	95	55	2152.45	435.96	109236.80	22.65	7.92	1.97	0.40
D	108	222	2729.55	1490.94	161440.05	25.27	6.71	1.69	0.92
Total						25.71	7.52	6.83	2.90

Table B-2: Average particle size and percentage area of the as-cast sample.

Sample	Count		Particle Size (μm^2)		Total Area (μm^2)	Average Particle Size (μm^2)		Percentage Area (%)	
	Cr	Nb	Cr	Nb		Cr	Nb	Cr	Nb
A	65	40	2319.28	1760.75	161188.36	35.68	44.02	1.44	1.09
B	60	41	2699.03	1890.22	150088.36	44.98	46.10	1.80	1.26
C	61	45	2706.32	1979.87	150900.36	44.37	44.00	1.79	1.31
D	70	40	2889.98	2098.23	151188.36	41.29	52.46	1.91	1.39
Total						41.58	46.64	6.94	5.05

Table B-3: Average particle size and percentage area of creep-tested sample 320

Sample	Count		Particle Size (μm^2)		Total Area (μm^2)	Average Particle Size (μm^2)		Percentage Area (%)	
	Cr	Nb	Cr	Nb		Cr	Nb	Cr	Nb
A	119	263	2772.50	1420.50	162313.56	23.30	5.40	1.71	0.88
B	83	117	3167.63	1550.14	161997.53	38.16	13.25	1.96	0.96
C	83	351	2441.65	1394.09	161599.46	29.42	3.97	1.51	0.86
D	59	77	2046.38	1089.08	161599.46	34.68	14.14	1.27	0.67
Total						31.39	9.19	6.44	3.37

Table B-4: Average particle size and percentage area of creep-tested sample 321

Sample	Count		Particle Size (μm^2)		Total Area (μm^2)	Average Particle Size (μm^2)		Percentage Area (%)	
	Cr	Nb	Cr	Nb		Cr	Nb	Cr	Nb
A	105	277	2707.76	1439.39	161599.46	25.79	5.20	1.68	0.89
B	87	112	2547.67	1127.74	161997.53	29.28	10.07	1.57	0.70
C	97	59	2160.16	444.96	109236.80	22.27	7.54	1.98	0.41
D	108	224	2730.88	1491.69	161440.05	25.29	6.66	1.69	0.92
Total						25.66	7.37	6.92	2.92

Table B-5: Average particle size and percentage area of creep-tested sample 322

Sample	Count		Particle Size (μm^2)		Total Area (μm^2)	Average Particle Size (μm^2)		Percentage Area (%)	
	Cr	Nb	Cr	Nb		Cr	Nb	Cr	Nb
A	105	283	3347.64	1377.02	161124.49	31.88	4.87	2.08	0.85
B	85	276	2243.33	1373.93	152520.92	26.39	4.98	1.47	0.90
C	97	278	2679.77	1393.85	161283.90	27.63	5.01	1.66	0.86
D	96	279	2756.92	1381.60	161915.02	28.72	4.95	1.70	0.85
Total						28.65	4.95	6.91	3.47

Table B-6: Average particle size and percentage area of creep-tested sample 326

Sample	Count		Particle Size (μm^2)		Total Area (μm^2)	Average Particle Size (μm^2)		Percentage Area (%)	
	Cr	Nb	Cr	Nb		Cr	Nb	Cr	Nb
A	64	134	2567.12	1330.28	161837.89	40.11	9.93	1.59	0.82
B	42	80	311.32	225.76	25908.71	7.41	2.83	1.20	0.87
C	76	159	2073.56	1494.64	161112.65	27.28	9.40	1.29	0.93
D	79	92	2682.38	1316.53	160387.41	33.95	14.31	1.67	0.82
Total						27.19	9.11	5.75	3.44

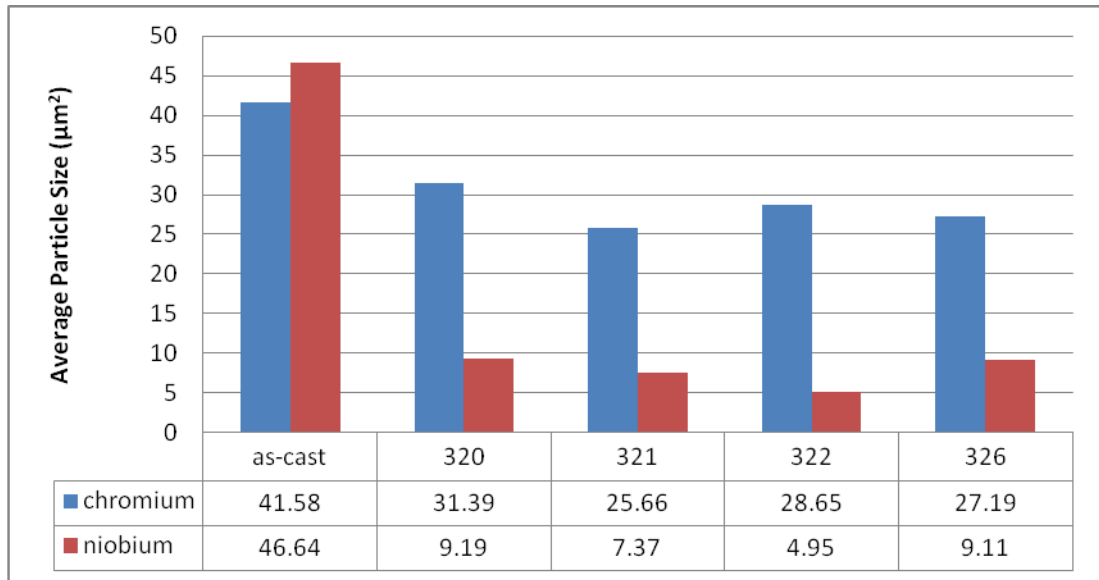


Figure B-1: Average particle size of Cr and Nb in the as-cast and creep-tested samples.

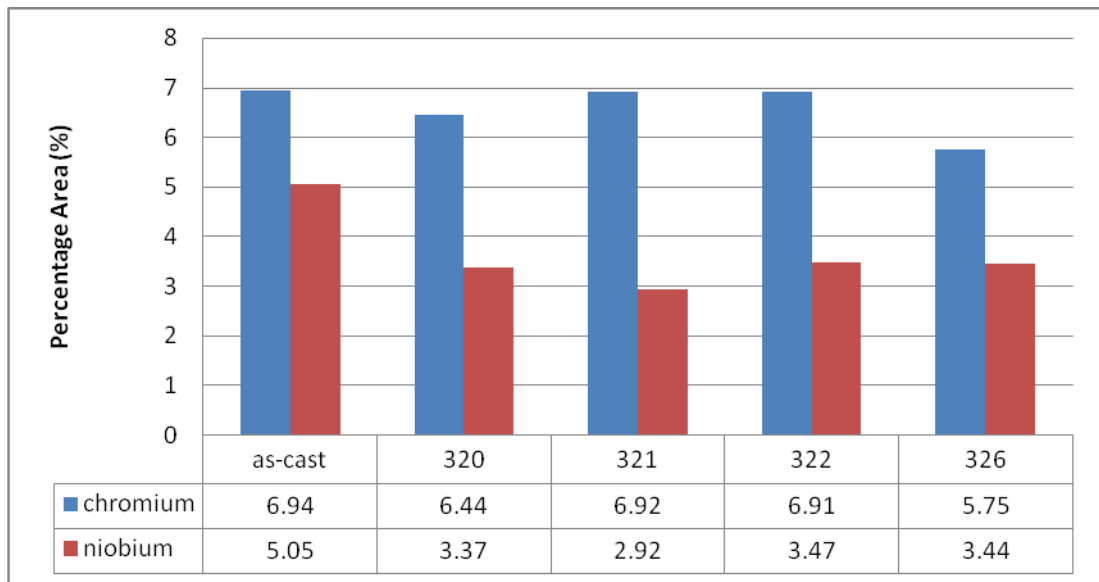


Figure B-2: Percentage area of Cr and Nb in the as-cast and creep-tested samples.

APPENDIX C
CONCLUSION

Table C-1: Elements, percent weight and percent atomic in as-cast Nb-rich precipitate obtained by spot mode

Element	Weight %	Atomic %
Ti K	0.60	0.24
Nb L	62.84	33.86

Table C-2: Elements, percent weight and percent atomic in creep-tested sample 321, Nb-rich precipitate by spot mode

Element	Weight %	Atomic %
Ti K	4.13	4.32
Nb L	43.78	8.82

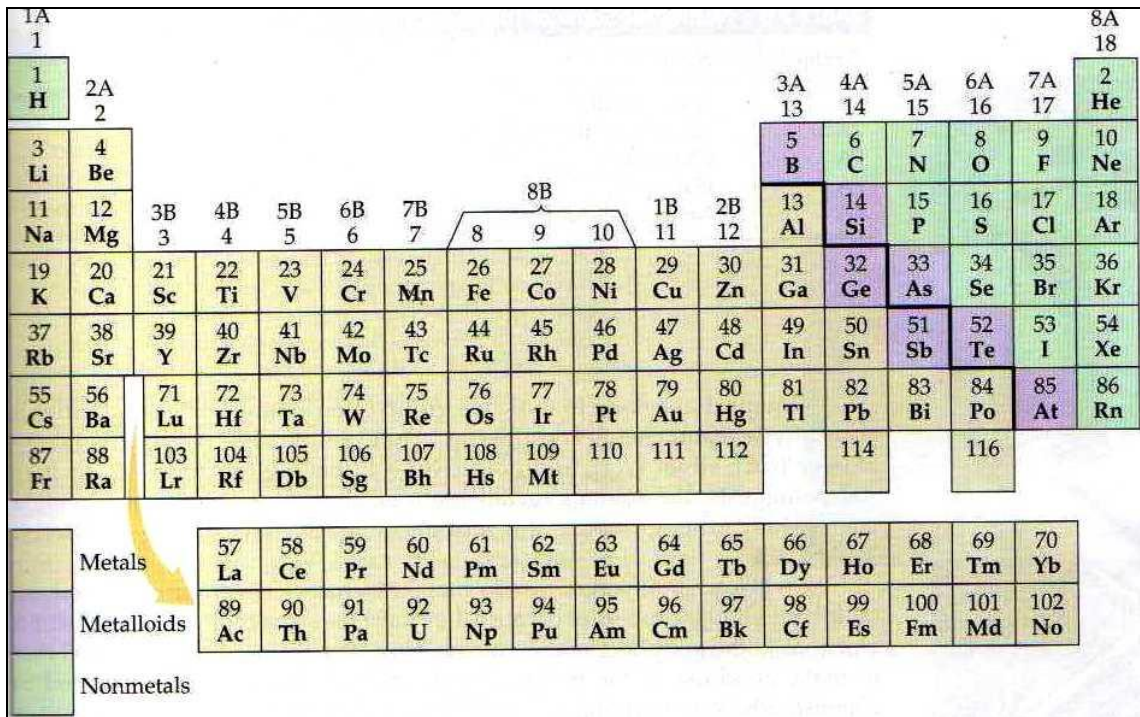


Figure C-1: Periodic table

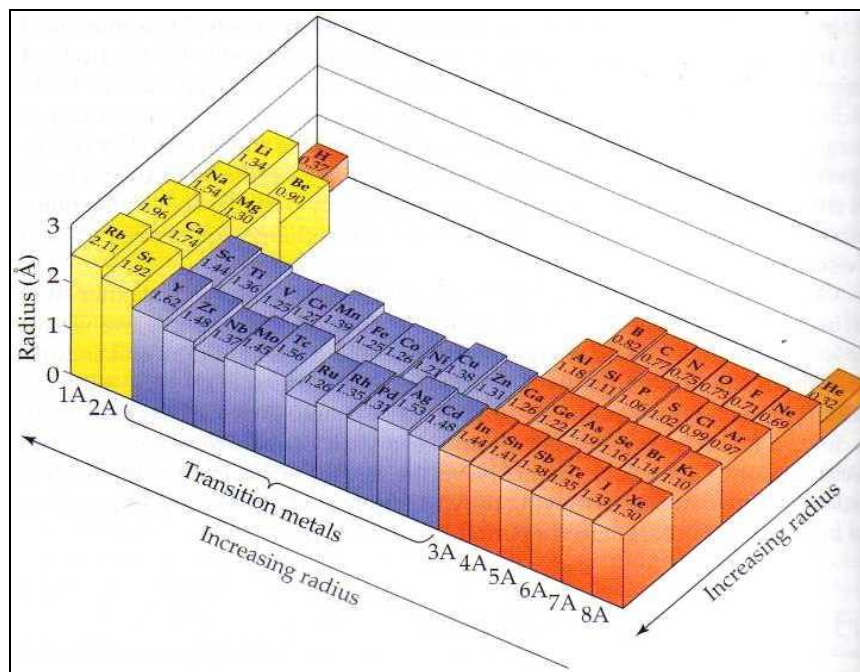


Figure C-2: Periodic table for the first 54 elements showing increasing radius direction

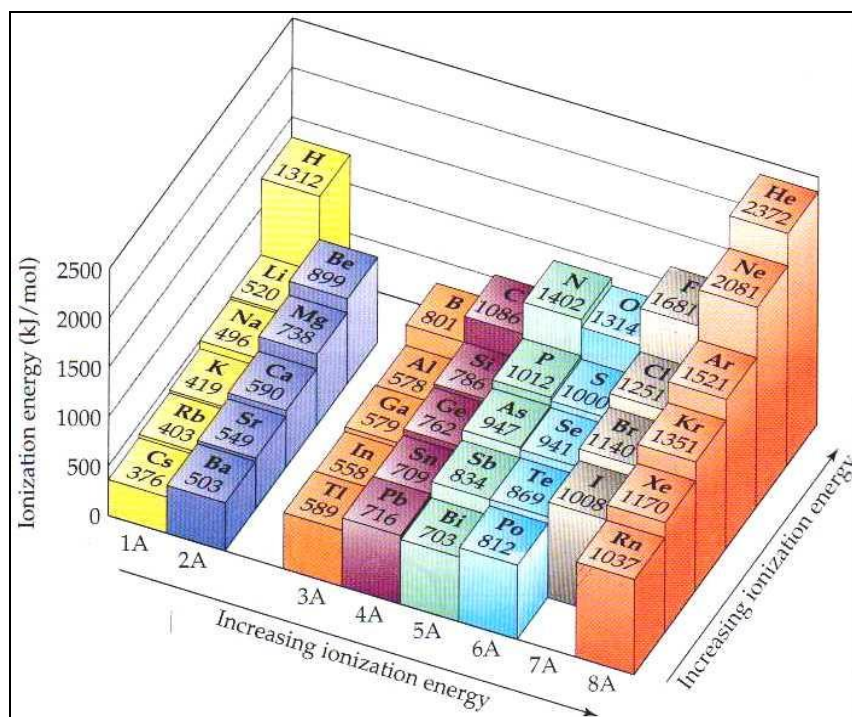


Figure C-3: Periodic table showing increasing ionization energy direction